Integrated Cellular and LEO-based Positioning and Synchronization under User Mobility

Yasaman Ettefagh, Sharief Saleh, *Member, IEEE*, Musa Furkan Keskin, *Member, IEEE*, Hui Chen, *Member, IEEE*, Gonzalo Seco-Granados, *Fellow, IEEE*, and Henk Wymeersch, *Fellow, IEEE*

***Abstract*—This paper investigates the localization, synchronization, and speed estimation of a mobile user equipment (UE) leveraging integrated terrestrial and non-terrestrial networks (NTNs), in particular low Earth orbit (LEO) satellites. We focus on a minimal setup in which the UE received signal from only one base station (BS) and one LEO satellite. We derive a generic signal model accounting for mobility, clock and frequency offsets, based on which a hierarchy of simplified models are proposed and organized by computational complexity. Estimation algorithms are developed for each model to facilitate efficient and accurate parameter recovery. Rigorous simulations validate the effectiveness of the proposed models, demonstrating their suitability across diverse scenarios. The findings highlight how the trade-off between complexity and performance can be optimized for varying deployment environments and application requirements, offering valuable insights for 6G positioning and synchronization systems under user mobility.**

***Index Terms*—cellular positioning, LEO satellites, mobility, non-terrestrial networks, synchronization**

I. Introduction

NON-terrestrial networks (NTNs) are becoming a critical component in the evolution of wireless communication systems, particularly in the transition from 5G to 6G. By integrating satellite systems, high altitude platform station (HAPS), and airborne networks, NTNs aim to provide ubiquitous and seamless global coverage, addressing connectivity gaps in under-served and remote regions [1], [2]. Beyond communication, NTNs have the potential to transform localization services by enabling global, high-precision positioning that is essential for a variety of emerging 6G applications [3], [4]. Among various NTN technologies, low Earth orbit (LEO) satellites stand out due to their low latency, high capacity, and scalability through large constellations [3], [5]. These capabilities make LEO satellites effective for critical localization applications such as autonomous driving (AD) and advanced driver-assistance systems (ADAS), where accuracy, reliability, and global availability are essential [2], [5]. By complementing terrestrial systems, NTNs are shaping the future of integrated localization and communication, enabling safe and efficient operation of autonomous vehicles, industrial automation, and other next-generation services [1], [3], [6], [7].

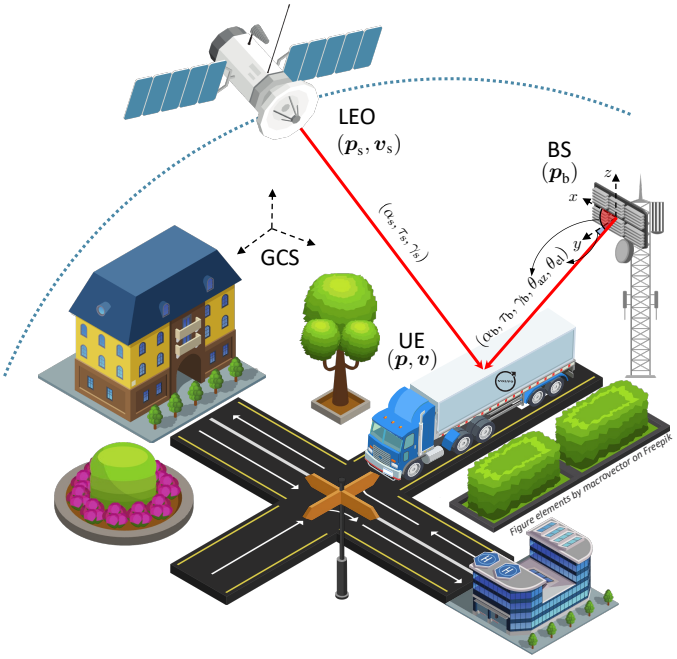


Fig. 1. TN-NTN integrated setup: the mobile UE is localized from coordinated downlink signals from the fixed BS and the mobile LEO satellite.

Positioning is increasingly central to the vision of 6G, enabling a wide range of advanced applications [8]. As part of this evolution, the design of integrated positioning systems that leverage the complementary strengths of terrestrial and non-terrestrial infrastructures has emerged as a key focus in realizing the next-generation communication and sensing ecosystem [2], [9]. Recent research has explored cellular localization frameworks that emphasize integrity, fault tolerance, and robust error bounding for safety-critical applications [10]. In parallel, hybrid positioning approaches that integrate terrestrial 5G and non-terrestrial systems, such as GNSS, have demonstrated promising sub-meter accuracy in field trials [11]. These applications demand high reliability and accuracy to ensure safe operation under diverse and challenging conditions, including urban environments with severe multipath interference and remote areas with limited terrestrial coverage.

Terrestrial networks (TNs) have been widely utilized for positioning services, but they face several critical limitations that impact accuracy and reliability [12]. Precise synchronization between base stations (BSs) and mobile devices is required

Copyright (c) 2026 IEEE. Personal use of this material is permitted. However, permission to use this material for any other purposes must be obtained from the IEEE by sending a request to pubs-permissions@ieee.org.

This work is supported by Vinnova FFI project 2023-02603 and by the Swedish Research Council (VR) under Grants 2022-03007 and 2024-04390, and in part by Grant PID2023-152820OB-I00 funded by MICIU/AEI/10.13039/501100011033 and by ERDF/EU, and the AGAUR - ICREA Academia Programme.

Yasaman Ettefagh is with the Department of Electrical Engineering, Chalmers University of Technology, 41296 Gothenburg, Sweden and also Volvo Technology AB, Gothenburg, Sweden (e-mail:ettefagh@chalmers.se; yasaman.ettefagh@volvo.com).

Sharief Saleh, Musa Furkan Keskin, Hui Chen and Henk Wymeersch are with the Department of Electrical Engineering, Chalmers University of Technology, 41296 Gothenburg, Sweden (emails: sharief@chalmers.se; furkan@chalmers.se; hui.chen@chalmers.se; henkw@chalmers.se).

Gonzalo Seco-Granados is with the Department of Telecommunications and Systems Engineering, Universitat Autonòma de Barcelona, CERES, IEEC, 08193 Bellaterra, Spain (e-mail: gonzalo.seco@uab.cat).

for accurate positioning, yet many cellular networks lack the stringent synchronization mechanisms needed for high-precision localization [13]. Another challenge is the limited coverage, as most positioning solutions require connection to at least four BSs, placing high demands on the infrastructure, compared to communication [14]. On the other hand, LEO satellite systems offer global coverage and have been proposed as a solution to enhance positioning services, considering both opportunistic form [15] and as part of 6G [4]. However, they also encounter specific limitations. The high mobility of LEO satellites leads to rapidly changing satellite geometries, causing high Doppler shifts [16], [17]. Furthermore, the beam patterns of LEO satellites, designed for communication purposes, often have narrow beam-widths for maximizing spectral efficiency, which conflicts with the broader, overlapping beams needed for accurate positioning. Interference management between overlapping beams in dense LEO constellations further complicates the system design [4].

Integrating terrestrial and NTN has attracted significant research interest due to the complementary strengths of these systems, both for communication [18]–[20] and for localization [9], [21]–[26]. Cellular networks, with their dense infrastructure and advanced signal processing capabilities, provide reliable positioning in urban areas, whereas NTNs, particularly LEO satellites, offer global coverage and resilience in rural or global navigation satellite system (GNSS)-denied environments. Recent studies have demonstrated the potential of 5G positioning reference signals to support integrated terrestrial-NTN scenarios, addressing challenges like Doppler shifts and interference in LEO-based networks [22], [23]. Fusion-based approaches, such as combining pseudorange and angle-of-arrival (AoA) measurements, have shown promise in enhancing positioning accuracy under low observability [25]. This integrated framework can bridge the performance gaps of individual systems, providing robust, precise positioning for emerging 6G applications. Nevertheless, this integration comes with challenges in terms of modeling, synchronization, and position estimation. In particular, in contrast to terrestrial-only or NTN-only positioning [4], jointly considering the terrestrial and non-terrestrial systems leads to high Doppler spread and delay spread, which in turn cause inter-carrier interference (ICI) and inter-symbol interference (ISI).

In this paper, we explore the fusion of NTN positioning, more specifically LEO positioning, with cellular positioning. The setup to be used comprises one multi-antenna BS together with a time and frequency-synchronous single antenna LEO satellite transmitting to a single-antenna mobile user equipment (UE) which has an unknown clock offset and frequency offset with respect to the BS and LEO satellite. The objective is to find the position of the UE as well as the magnitude of velocity (speed), and clock and frequency offsets. The contributions of this paper are listed as follows:

- **Unified discrete-time generative model for integrated TN–NTN OFDM:** We derive a generative model that jointly captures BS-induced and LEO-induced Doppler (slow and fast time), intersubcarrier Doppler, ICI, time-varying AoD, and UE clock asynchrony. While each physical effect is individually well studied, their *combined* interaction in an integrated TN–NTN OFDM architecture, using shared time-frequency resources, has not been explicitly modeled in prior work. This unified treatment forms the basis for systematic simplification and estimator design.
- **Systematic hierarchy of simplified models:** Starting from the unified generative model, we construct a structured hierarchy of four simplified models by progressively removing classes of impairments. This creates a consistent reduction path: (i) *Comm* removes all Doppler-related terms (slow-time, intersubcarrier, and ICI), yielding a constant-phase OFDM model. (ii) *SlowD* reintroduces only the slow-time Doppler component, modeling phase evolution across OFDM symbols. (iii) *CCFODnoICI* additionally incorporates intersubcarrier Doppler effects [27], while still neglecting ICI. (iv) *CCFOD* finally restores both slow- and fast-time Doppler, including ICI [27], [28]. While the individual physical effects have been studied in classical OFDM and LEO-only links, this *progressive, TN–NTN-specific* hierarchy is new and enables a principled comparison of accuracy and computational complexity across modeling fidelities.
- **Low-complexity estimators with Doppler–AoD decoupling:** For each simplified model, we develop practical estimators for delays, Doppler shifts, and AoD. The estimators explicitly exploit the structure of the TN–NTN model, including (i) the use of beamformer phase repetition to decouple Doppler and AoD, (ii) partial compensation of intersubcarrier Doppler using the satellite–BS Doppler proxy, and (iii) tractable reconstruction of the BS path in the presence of ICI. These elements are not present in prior LEO-only positioning algorithms.
- **Model evaluation and selection via CRB and MCRB:** We evaluate the simplified models using Cramér-Rao bound (CRB) and misspecified Cramér-Rao bound (MCRB) analysis to quantify the impact of model mismatch. This provides analytical conditions under which simpler models achieve performance comparable to more complex ones, reducing the need for Monte Carlo simulations. The resulting insights support principled model selection for different deployment scenarios and complexity constraints.

While CFO, Doppler, and clock offset have each been treated in isolation in prior LEO-only [17] and jointly modeled in waveform-agnostic settings [26], their joint interaction in an integrated TN–NTN setting with OFDM has not been explicitly modeled. In contrast to prior work, our generative model captures (i) the simultaneous presence of BS-induced and satellite-induced Doppler with different orders and time scales, (ii) the coupling between CFO, Doppler, and clock offset in both slow-time and fast-time domains, and (iii) the resulting phase distortions across OFDM symbols and subcarriers. This unified treatment is required to derive the hierarchy of models and the associated estimators.

Notation: Vectors and matrices are shown by bold-face lower-case and bold-face upper-case letters respectively. The notations $(.)^{\mathsf{T}}$ and $(.)^{\mathsf{H}}$ represent transpose and hermitian transpose. All one vector with size n denoted by $\mathbf{1}_n$. The L2 norm of a vector is shown by $\|.\|$. The Hadamard product and convolution are represented by $\odot$ and $*$ respectively. The set of real numbers and complex numbers are shown by $\mathbb{R}$ and $\mathbb{C}$ respectively. The delta Dirac function is represented by

$\delta(.)$. The function rect(x) is defined such that rect$(x) = 1$ for $0 < x < 1$ and is 0 otherwise. The $(m,n)^{\text{th}}$ element of the matrix $\boldsymbol{A}$ is referred to by $[\boldsymbol{A}]_{(m,n)}$ and the notation $\tilde{(.)}$ represents a passband signal.

II. System Model

A. Scenario

We consider a system consisting of a BS equipped with a uniform planar array (UPA) of $\sqrt{L} \times \sqrt{L}$ antennas located at known location $\boldsymbol{p}_{\text{b}} \in \mathbb{R}^3$, a LEO satellite with a directional antenna with known and varying location and velocity $\boldsymbol{p}_{\text{s}}(t) \in \mathbb{R}^3$ and $\boldsymbol{v}_{\text{s}}(t) \in \mathbb{R}^3$, respectively, and a single-antenna UE. The setup is illustrated in Fig. 1. The UE travels at a constant velocity $\boldsymbol{v} \in \mathbb{R}^3$ with known direction $\boldsymbol{v}/\|\boldsymbol{v}\|$ [1], but unknown speed $\|\boldsymbol{v}\|$ and unknown initial location $\boldsymbol{p}_0 \in \mathbb{R}^3$. As a result, the trajectory of the UE is given by $\boldsymbol{p}(t) = \boldsymbol{p}_0 + \boldsymbol{v}t$. The clock oscillators at the BS and the satellite are assumed to be synchronized to a common global reference. The clock oscillator at the UE is assumed to have an unknown initial clock offset, denoted as $\Delta_{t,0}$, relative to the clock oscillators at the BS and the satellite. Additionally, the UE's clock oscillator introduces a carrier frequency offset (CFO) η which is treated as an unknown.

B. Signal and Channel Model

We assume the positioning task is performed using one transmission consisting M orthogonal frequency division multiplexing (OFDM) symbols, each comprising N subcarriers (with a subcarrier spacing of Δ_f). We assign the even and the odd subcarriers to the signal transmitted by the BS and the satellite, respectively. The baseband transmit signal at the base station ($\boldsymbol{z}_{\text{b}}(t) \in \mathbb{C}^L$) is

$$\boldsymbol{z}_{\text{b}}(t) = \boldsymbol{w}(t) x_{\text{b}}(t) = \boldsymbol{w}(t) \sum_{m=0}^{M-1} x_{\text{b},m}(t), \tag{1}$$

where

$$x_{\text{b},m}(t) = \frac{1}{\sqrt{N}} \sum_{n=0,\text{even } n}^{N-1} x_{n,m} e^{j2\pi n \Delta_f (t - mT_s)} q(t - mT_s).$$

Here, $q(t) = \text{rect}(t/T_s)$,[2] $\boldsymbol{w}(t) \in \mathbb{C}^L$ is the time-varying precoding matrix, $x_{n,m}$ is the pilot at the n^{th} subcarrier of the m^{th} symbol. The total symbol duration is $T_s = T_0 + T_{\text{cp}}$, where $T_0 = 1/\Delta_f$ is the elementary symbol duration, and T_{cp} is the cyclic prefix duration. Then the transmit signal upconverted to the carrier frequency f_c is $\tilde{\boldsymbol{z}}_{\text{b}}(t) = \Re\{\boldsymbol{z}_{\text{b}}(t) e^{j2\pi f_c t}\}$.

The time-varying channel between the BS and the UE ($\tilde{\boldsymbol{h}}_{\text{b}}(t,\tau) \in \mathbb{C}^L$) can be expressed as follows, for the l^{th} BS antenna:

$$\tilde{h}_{\text{b},l}(t,\tau) = [\tilde{\boldsymbol{h}}_{\text{b}}(t,\tau)]_l = \alpha_{\text{b}}(t) \delta(\tau - \tau^p_{\text{b},l}(t)), \tag{2}$$

where $\alpha_{\text{b}}(t)$ denotes the time-varying real-valued channel gain between the BS and the UE and $\tau^p_{\text{b},l}(t)$ expresses[3] the time-varying propagation delay between the l^{th} antenna at the BS and the UE. Therefore, the passband noise-free received signal at the UE can be written as

$$\tilde{y}_{\text{b}}(t) = \alpha_{\text{b}}(t) \sum_{l=1}^{L} \tilde{z}_{\text{b},l}(t - \tau^p_{\text{b},l}(t)). \tag{3}$$

Similar to the BS-UE transmission, the baseband transmit signal at the satellite is $x_{\text{s}}(t) = \sum_{m=0}^{M-1} x_{\text{s},m}(t)$, where

$$x_{\text{s},m}(t) = \frac{1}{\sqrt{N}} \sum_{n=0,\text{odd } n}^{N-1} x_{n,m} e^{j2\pi n \Delta_f (t - mT_s)} q(t - mT_s).$$

Here, $x_{n,m}$ is the pilot signal transmitted by the satellite. Then the upconverted transmit signal is $\tilde{s}_{\text{s}}(t) = \Re\{x_{\text{s}}(t) e^{j2\pi f_c t}\}$. We denote the time-varying channel between the satellite and the UE by $\tilde{h}_{\text{s}}(t,\tau) = \alpha_{\text{s}}(t) \delta(\tau - \tau^p_{\text{s}}(t))$, where $\alpha_{\text{s}}(t)$ and $\tau^p_{\text{s}}(t)$ denote the time-varying channel gain and propagation delay between the satellite and the UE. Therefore, the noise-free received signal at the UE from the satellite will be

$$\tilde{y}_{\text{s}}(t) = \alpha_{\text{s}}(t) \tilde{s}_{\text{s}}(t - \tau^p_{\text{s}}(t)). \tag{4}$$

Finally, the total passband received signal will be

$$\tilde{y}(t) = \tilde{y}_{\text{b}}(t) + \tilde{y}_{\text{s}}(t) + \tilde{n}(t), \tag{5}$$

where $\tilde{n}(t)$ is the passband additive white Gaussian noise (AWGN) at the UE, with power spectral density N_0.

C. Geometric Relations

The time-varying propagation delay between the l^{th} antenna of the BS and the UE is given by

$$\tau^p_{\text{b},l}(t) = \tau^p_{\text{b}}(t) + \tau^p_l(t), \tag{6}$$

where $\tau^p_{\text{b}}(t) = \|\boldsymbol{p}(t) - \boldsymbol{p}_{\text{b}}\|/c$ is the delay between the BS phase center and the UE, and c is the speed of light. Assuming the UE is located in the far-field region of the BS, the relative delay (or advance) of the l^{th} antenna element with respect to the phase center is $\tau^p_l(t) = -(\boldsymbol{u}(\boldsymbol{\theta}(t))^{\mathsf{T}} \boldsymbol{q}_l)/c$, where $\boldsymbol{q}_l \in \mathbb{R}^3$ is the known position of the l^{th} antenna element with respect to the BS phase center. The unit direction vector $\boldsymbol{u}(\boldsymbol{\theta}(t)) \in \mathbb{R}^3$ captures the orientation of the UE with respect to the BS, and is defined as $\boldsymbol{u}(\boldsymbol{\theta}(t)) = [\cos(\theta_{\text{el}}(t)) \cos(\theta_{\text{az}}(t)),\ \cos(\theta_{\text{el}}(t)) \sin(\theta_{\text{az}}(t)),\ \sin(\theta_{\text{el}}(t))]^{\mathsf{T}}$, where $\boldsymbol{\theta}(t) = \left[\theta_{\text{el}}(t), \theta_{\text{az}}(t)\right]^{\mathsf{T}} \in \mathbb{R}^2$ is the time-varying 2D angle-of-departure (AoD) in the global coordinate system. These angles are computed based on the relative position vector $\boldsymbol{r}_{\text{b}}(t) = \boldsymbol{p}(t) - \boldsymbol{p}_{\text{b}}$ from the BS to the UE, as

$$\theta_{\text{el}}(t) = \arcsin\left(\frac{[\boldsymbol{r}_{\text{b}}(t)]_3}{\|\boldsymbol{r}_{\text{b}}(t)\|}\right), \tag{7}$$

$$\theta_{\text{az}}(t) = \text{atan2}\left([\boldsymbol{r}_{\text{b}}(t)]_2, [\boldsymbol{r}_{\text{b}}(t)]_1\right). \tag{8}$$

Finally, the time-varying propagation delay between the satellite and the UE is given by $\tau^p_{\text{s}}(t) = \|\boldsymbol{p}(t) - \boldsymbol{p}_{\text{s}}(t)\|/c$.

D. Problem Statement

The UE should determine its initial position $\boldsymbol{p}_0$ and its speed $\|\boldsymbol{v}\|$, from the observation $\tilde{y}(t)$ in (5), in the presence of the unknown and time-varying channel parameters, and without being a priori synchronized to the network (the BS and the satellite). The details of the UE-network asynchrony will be elaborated in the next section. For ease of reference, the parameters introduced in the following sections are summarized in Table I.

[1]The direction can be estimated using inertial sensors (e.g., inertial measurement units (IMUs)) through dead reckoning or short-term motion tracking, even without reliable GNSS.

[2]In case of using a more practical root-raised cosine (RRC) pulse instead of a rectangular pulse, we need to apply matched filters at the receiver.

[3]The superscript "p" indicates that the delay is purely due to propagation, distinguishing it from the total effective delay values that will be introduced later.

III. Generative and Simplified Models

In this section, we begin by introducing the notion of time-varying clock bias; then, we derive the generative model used to generate observations for the localization task. To assist algorithm development, we propose four distinct simplified models, some of which are widely used in the literature.

A. Clock and Frequency Offset

Due to the imperfect clock oscillator at the UE, the notion of time at the UE differs from that at the BS and satellite. The time reference of the receiver is denoted by t' and is supposed to be related to the time reference at the transmitter through

$$t' = t/(1-\eta) + \Delta_{t,0}, \tag{9}$$

where t represents the network reference time and $\Delta_{t,0}$ is the initial clock offset. Hence, for $|\eta| \ll 1$ it holds that the time-varying offset $\Delta_t(t) = t' - t$ can be expressed as $\Delta_t(t) \approx \eta t + \Delta_{t,0}$ [29].

B. Generative Model

1) Continuous-time Model: The received passband signal in the global time reference t in (3) and (4) has the below contributions from the BS-UE path and satellite-UE path (see Appendix A):

$$\tilde{y}_{\mathrm{b}}(t) = \tag{10}$$
$$\Re\{\alpha_{\mathrm{b}}(t)\boldsymbol{a}^{\mathsf{T}}(\boldsymbol{\theta}(t))\boldsymbol{w}(t-\tau_{\mathrm{b}}^{p}(t))x_{\mathrm{b}}\left(t-\tau_{\mathrm{b}}^{p}(t)\right)e^{j2\pi f_c\left(t-\tau_{\mathrm{b}}^{p}(t)\right)}\}$$

where the array steering vector $\boldsymbol{a}(\boldsymbol{\theta}(t))$ is given by $[\boldsymbol{a}(\boldsymbol{\theta}(t))]_l = \exp(j(2\pi/\lambda)\boldsymbol{u}^{\mathsf{T}}(\boldsymbol{\theta}(t))\boldsymbol{q}_l)$ [30], and

$$\tilde{y}_{\mathrm{s}}(t) = \Re\big\{\alpha_{\mathrm{s}}(t)x_{\mathrm{s}}\left(t-\tau_{\mathrm{s}}^{p}(t)\right)e^{j2\pi f_c(t-\tau_{\mathrm{s}}^{p}(t))}\big\}. \tag{11}$$

It is possible to approximate $\tau_i^p(t)$, (with $i \in \{\mathrm{b},\mathrm{s}\}$) as (see Appendix B)

$$\begin{aligned}\tau_i^p(t) &= \frac{\|\boldsymbol{p}(t)-\boldsymbol{p}_i(t)\|}{c} \approx \frac{\|\boldsymbol{p}_0-\boldsymbol{p}_i\|}{c} + \frac{v_{i,\mathrm{u}}}{c}t + \frac{a_{i,\mathrm{u}}}{2c}t^2 \\ &= \tau_i^p + \psi_i t + \frac{1}{2}\mu_i t^2,\end{aligned} \tag{12}$$

and $\tau_i^p = \|\boldsymbol{p}_0-\boldsymbol{p}_i\|/c$, $\psi_i = v_{i,\mathrm{u}}/c$, $v_{i,\mathrm{u}} = (\boldsymbol{p}_0-\boldsymbol{p}_i)^{\mathsf{T}}\boldsymbol{v}_{i,\mathrm{u}}/\|\boldsymbol{p}_0-\boldsymbol{p}_i\|$, $\mu_i = a_{i,\mathrm{u}}/c$, and $a_{i,\mathrm{u}} = (\|\boldsymbol{v}_{i,\mathrm{u}}\|^2 - v_{i,\mathrm{u}}^2)/\|\boldsymbol{p}_0-\boldsymbol{p}_i\|$, in which $\boldsymbol{v}_{\mathrm{b,u}} = \boldsymbol{v}$ and $\boldsymbol{v}_{\mathrm{s,u}} = (\boldsymbol{v}+\boldsymbol{v}_{\mathrm{E}})-\boldsymbol{v}_{\mathrm{LEO}}$, where $\boldsymbol{v}_{\mathrm{E}}$ denotes the Earth rotational velocity.

We now rewrite the received signal *in the receiver's time domain* t' by substituting $t = (t'-\Delta_{t,0})(1-\eta)$ according to (9) and using (12)

$$\begin{aligned}\tilde{y}'(t') &= \tilde{y}'_{\mathrm{b}}(t') + \tilde{y}'_{\mathrm{s}}(t') + \tilde{n}'(t') \\ &= \Re\big\{\alpha'_{\mathrm{b}}(t')\boldsymbol{a}'^{\mathsf{T}}(\boldsymbol{\theta}'(t'))\boldsymbol{w}'(t_b)x'_{\mathrm{b}}\left(t_b\right)e^{j2\pi f_c t_b} \\ &\quad + \alpha'_{\mathrm{s}}(t')x'_{\mathrm{s}}\left(t_s\right)e^{j2\pi f_c t_s} + \tilde{n}'(t')\big\},\end{aligned} \tag{13}$$

where $\alpha'_{\mathrm{b}}(t') = \alpha_{\mathrm{b}}((t'-\Delta_{t,0})(1-\eta))$, $\boldsymbol{\theta}'(t') = \boldsymbol{\theta}((t'-\Delta_{t,0})(1-\eta))$. To ease the notation, we have introduced $t_b = (1-\gamma_b)t' - \tau_b - \epsilon_b t'^2$, $t_s = (1-\gamma_s)t' - \tau_s - \epsilon_s t'^2$ and define $\boldsymbol{w}'(t_b) = \boldsymbol{w}((1-\gamma_b)t' - \tau_b - \epsilon_b t'^2)$, and

$$\gamma_i = \psi_i(1-\eta) + \eta - \mu_i(1-\eta)^2\Delta_{t,0}, \tag{14a}$$
$$\epsilon_i = 1/2\mu_i(1-\eta)^2, \tag{14b}$$
$$\tau_i = \tau_i^p + \Delta_{t,0}(1-\eta)(1-\psi_i) + 1/2\mu_i\Delta_{t,0}^2(1-\eta)^2, \tag{14c}$$

where $i \in \{b,s\}$. Here, γ_i, ϵ_i, and τ_i can be interpreted as the effective Doppler shift, effective Doppler rate, and effective delay, respectively, in a system affected by clock offset, carrier frequency offset, and time-varying Doppler. This completes the continuous-time generative model, accounting for both first- and second-order Doppler effects as well as the asynchrony between the UE and the network.

TABLE I
List of Parameters

Symbol	Description
UE	
$\boldsymbol{p}_0$	Initial position of the UE
$\boldsymbol{v}$	Velocity vector of the UE
$\|\boldsymbol{v}\|$	Speed of the UE
$\boldsymbol{p}(t)$	Position of the UE at time t
$\Delta_{t,0}$	Initial clock offset of the UE
t'	Local time at the UE
$\Delta_t(t)$	Time-varying clock offset
η	CFO of the UE
BS	
$\boldsymbol{p}_{\mathrm{b}}$	Position of the BS
$\boldsymbol{q}_l$	Position of the l^{th} BS antenna element
$\boldsymbol{\theta}(t)$	2D AoD $(\theta_{\mathrm{el}}(t), \theta_{\mathrm{az}}(t))$ at time t
$\boldsymbol{r}_{\mathrm{b}}(t)$	Vector from the BS to the UE
$\tau_{\mathrm{b},l}^{p}(t)$	Propagation delay from l^{th} BS antenna to UE
$\tau_{\mathrm{b}}^{p}(t)$	Propagation delay from BS center to UE
$\tau_{l}^{p}(t)$	Relative delay from l^{th} antenna to BS center
Satellite	
$\boldsymbol{p}_{\mathrm{s}}(t)$	Position of the satellite at time t
$\boldsymbol{v}_{\mathrm{s}}$	Velocity of the satellite
$\tau_{\mathrm{s}}^{p}(t)$	Propagation delay from satellite to UE
τ_{s}^{res}	Initial residual delay after satellite timing advance
Propagation and Doppler Terms	
$\tau_i^p(t)$	Propagation delay from node $i \in \{\mathrm{b},\mathrm{s}\}$ to UE
τ_i^p	Initial propagation delay from node i to UE
ψ_i	First-order Doppler term for node i
μ_i	Second-order Doppler term for node i
γ_i	Effective Doppler shift for node i
ϵ_i	Effective Doppler rate for node i
τ_i	Effective initial delay for node i
BS-Satellite Relative Terms	
$\boldsymbol{v}_{\mathrm{b}}$	Relative velocity between BS and satellite
$\bar{\psi}_{\mathrm{b}}$	Proxy Doppler term for satellite-BS path
τ_{b}	Estimated delay between BS and satellite

2) Doppler and Time Precompensation: Based on (13), the received frequency through the BS-UE path is $f_c(1-\gamma_b)$ and through the satellite-UE path is $f_c(1-\gamma_s)$. This results in a significant Doppler spread of the received signal due to high velocity of the LEO satellite, which causes limitations in low-pass filtering prior to sampling at the receiver. Although γ_b is unknown and much smaller than γ_s, a significant portion of γ_s can be determined from the known satellite velocity and position, as well as the known BS position, under the assumption that the UE is in close proximity to the BS. Consequently, it is feasible to apply a frequency (Doppler) precompensation at the satellite prior to transmission, thereby rendering the Doppler shifts in the received signals through different paths more comparable and reducing the overall Doppler spread. To achieve this, a proxy for γ_s, denoted by $\bar{\psi}_{\mathrm{sb}}$, can be estimated as follows (where the subscript 'sb' represents satellite-BS path):

$$\bar{\psi}_{\mathrm{sb}} = v_{\mathrm{sb}}/c, \tag{15}$$
$$v_{\mathrm{sb}} = (\boldsymbol{p}_{\mathrm{b}}-\boldsymbol{p}_{\mathrm{s}})^{\mathsf{T}}\boldsymbol{v}_{\mathrm{sb}}/\|\boldsymbol{p}_{\mathrm{b}}-\boldsymbol{p}_{\mathrm{s}}\|, \tag{16}$$
$$\boldsymbol{v}_{\mathrm{sb}} = \boldsymbol{v}_{\mathrm{E}} - \boldsymbol{v}_{\mathrm{LEO}}. \tag{17}$$

Then, we can utilize $\bar{\psi}_{\mathrm{sb}}$ to adjust the transmit frequency at the satellite to $\bar{f}_c = f_c/(1-\bar{\psi}_{\mathrm{sb}})$. With this Doppler precompensation, the received frequency in the satellite-UE path is changed from $f_c(1-\gamma_s)$ to $f_c(1-\gamma_s)/(1-\bar{\psi}_{\mathrm{sb}})$.

Similarly, in the time domain, the propagation delay experienced by the signal in the satellite-UE path is considerably larger than that in the BS-UE path. Nevertheless, a significant portion of the satellite-UE propagation delay is already known from the satellite and BS positions, as well as the UE's proximity to the BS. Hence, it is possible to apply timing advance at the satellite to reduce the delay spread in the received signal. Analogous to Doppler precompensation, a rough estimate of τ_{s}^{p} can be obtained as

$$\tau_{\mathrm{sb}} = \|\boldsymbol{p}_{\mathrm{b}} - \boldsymbol{p}_{\mathrm{s}}\|/c, \tag{18}$$

and we can then apply a timing advance of τ_{sb} to the satellite transmit signal $s(t)$, expressed as

$$\tilde{\bar{s}}_{\mathrm{s}}(t) = \Re\{x_{\mathrm{s}}(t+\tau_{\mathrm{sb}})e^{j2\pi f_c(t+\tau_{\mathrm{sb}})}\}. \tag{19}$$

In this case, τ_s is replaced by τ_s^{res} [4] in (13) defined as follows:

$$\tau_s^{\mathrm{res}} = \tau_{\mathrm{s}} - \tau_{\mathrm{sb}}. \tag{20}$$

3) Down-Conversion: To down-convert to the baseband, the clock oscillator at the UE generates $e^{-j2\pi f_c t'}$. Consequently, after removing the constant phases, the baseband signal becomes:

$$\begin{aligned} y'(t') = \tilde{y}'(t')e^{-j2\pi f_c t'} &= \alpha'_{\mathrm{b}}(t')z(t')\sum_{m=0}^{M-1}\frac{1}{\sqrt{N}}\sum_{n=0,\ \text{even n}}^{N-1} \\ &x_{n,m}e^{j2\pi n\Delta_f(t_b-mT_s)}e^{-j2\pi f_c\left(\gamma_b t'+\epsilon_b t'^2\right)}q(t_b-mT_s) \\ &+\alpha'_{\mathrm{s}}(t')\sum_{m=0}^{M-1}\frac{1}{\sqrt{N}}\sum_{n=0,\ \text{odd n}}^{N-1} x_{n,m}e^{j2\pi n\Delta_f(t_s^{\mathrm{res}}-mT_s)} \\ &\times e^{-j2\pi\bar{f}_c\left(\gamma_s t'+\epsilon_s t'^2\right)}e^{j2\pi(\bar{f}_c-f_c)t'}q(t_s^{\mathrm{res}}-mT_s)+n'(t'), \end{aligned} \tag{21}$$

where $z(t') = \boldsymbol{a}^{\mathsf{T}}(\boldsymbol{\theta}(t'))\boldsymbol{w}'(t_b)$ and $t_s^{\mathrm{res}} = (1-\gamma_s)t' - \tau_s^{\mathrm{res}} - \epsilon_s t'^2$.

4) Discrete-time Model: To obtain the discrete-time received signal, we first apply analog-domain low-pass filtering to suppress out-of-band components, and then sample (21) at time instants $t' = mT_s + T_{\mathrm{cp}} + kT_0/N + \tau_0$, where $k = 0, 1, \ldots, N-1$, and

$$\tau_0 = \min\left(\tau_{\mathrm{b}}/(1-\eta), \tau_{\mathrm{s}}/(1-\eta)\right), \tag{22}$$

represents the smallest delay in the receiver's time domain that ensures the first OFDM symbol is fully captured. In (22), τ_{b} and τ_{s} are defined in (14c). Let us assume that τ_0 is detectable (through time acquisition in [31]) and hence we can start the receiver's clock at τ_0. We can take N samples from each OFDM symbol, resulting in $\mathbf{Y} = [\mathbf{y}_0, \cdots, \mathbf{y}_{M-1}] \in \mathbb{C}^{N\times M}$ where $\mathbf{y}_m$ is defined as

$$\mathbf{y}_m = \mathbf{y}_{\mathrm{b},m} + \mathbf{y}_{\mathrm{s},m} + \mathbf{n}_m, \tag{23}$$

with

$$\begin{aligned} \mathbf{y}_{\mathrm{b},m} = \sqrt{P_{\mathrm{b}}}[\boldsymbol{A}_{\mathrm{b}}]_{(:,m)} \odot [\boldsymbol{Z}]_{(:,m)} \odot \Bigg(&\mathbf{D}_{\mathrm{b}}^{q}(\gamma_b,\epsilon_b) \\ &\times \mathbf{F}_{m,\mathrm{b}}^{q}(\gamma_b,\epsilon_b)\Big(\boldsymbol{i}_{m,\mathrm{b}}^{q}(\gamma_b,\epsilon_b) \odot \Big(\big(\boldsymbol{q}_{\mathrm{b}}(\gamma_b)\odot\boldsymbol{b}_{\mathrm{b}}(\tau_b)\big) \\ &\times [\mathbf{c}_{\mathrm{b}}^{q}(\gamma_b,\epsilon_b)]_m\Big)\Big)\Bigg) \odot \mathbf{H}_{\mathrm{b}}^{q}(\epsilon_b), \end{aligned} \tag{24}$$

$$\mathbf{y}_{\mathrm{s},m} = \sqrt{P_{\mathrm{s}}}[\boldsymbol{A}_{\mathrm{s}}]_{(:,m)} \odot \Bigg(\mathbf{D}_{\mathrm{s}}^{q}(\gamma_s,\epsilon_s)\mathbf{F}_{\mathrm{s}}^{q}(\gamma_s,\epsilon_s)\times \Big(\boldsymbol{i}_{m,\mathrm{s}}^{q}(\gamma_s,\epsilon_s) \odot \Big(\big(\boldsymbol{q}_{\mathrm{s}}(\gamma_s)\odot\boldsymbol{b}_{\mathrm{s}}(\tau_s^{\mathrm{res}})\big)[\mathbf{c}_{\mathrm{s}}^{q}(\gamma_s,\epsilon_s)]_m\Big)\Big)\Bigg) \odot \mathbf{H}_{\mathrm{s}}^{q}(\epsilon_s). \tag{25}$$

The superscript 'q' is used to underscore that the corresponding matrices/vectors contain quadratic terms, which originate from (12). The different matrices defined above are used to capture the different effects:

- *Time variations:* $[\boldsymbol{A}_{\mathrm{b}}]_{(:,m)}$, $[\boldsymbol{A}_{\mathrm{s}}]_{(:,m)}$ and $[\boldsymbol{Z}]_{(:,m)}$ comprise the samples of $\alpha'_{\mathrm{b}}(t')$, $\alpha'_{\mathrm{s}}(t')$ and $z(t')$, respectively.
- *Inter-carrier interference:* The diagonal matrices $\mathbf{D}_{\mathrm{b}}^{q}(\gamma_b,\epsilon_b) \in \mathbb{C}^{N\times N}$ and $\mathbf{D}_{\mathrm{s}}^{q}(\gamma_s,\epsilon_s) \in \mathbb{C}^{N\times N}$ are the main source of ICI in the BS-UE and satellite-UE paths, respectively. The k^{th} diagonal element of each matrix is defined as

$$\begin{aligned} &[\mathbf{D}_{\mathrm{b}}^{q}(\gamma_b,\epsilon_b)]_{k,k} = \\ &e^{-j2\pi f_c(\gamma_b T_0 k/N+\epsilon_b T_0^2 k^2/N^2+2\epsilon_b T_{\mathrm{cp}}T_0 k/N)}, \end{aligned} \tag{26}$$

$$\begin{aligned} [\mathbf{D}_{\mathrm{s}}^{q}(\gamma_s,\epsilon_s)]_{k,k} = e^{-j2\pi f_c(1-(1-\gamma_s)/(1-\bar{\psi}_{\mathrm{sb}}))T_0 k/N} \\ \times e^{-j2\pi f_c(\epsilon_s T_0^2/(1-\bar{\psi}_{\mathrm{sb}})k^2/N^2+2\epsilon_s T_{\mathrm{cp}}T_0/(1-\bar{\psi}_{\mathrm{sb}})k/N)}. \end{aligned} \tag{27}$$

- *Slow-time Doppler:* The slow-time effect in BS-UE path and satellite-UE path are denoted by $\mathbf{c}_{\mathrm{b}}^{q}(\gamma_b,\epsilon_b)$ and $\mathbf{c}_{\mathrm{s}}^{q}(\gamma_s,\epsilon_s)$ respectively and defined as

$$[\mathbf{c}_{\mathrm{b}}^{q}(\gamma_b,\epsilon_b)]_m = e^{-j2\pi f_c(\gamma m T_s+\epsilon_b m^2 T_s^2+2\epsilon_b m T_s T_{\mathrm{cp}})}, \tag{28}$$

$$\begin{aligned} [\mathbf{c}_{\mathrm{s}}^{q}(\gamma_s,\epsilon_s)]_m = e^{-j2\pi f_c((1-(1-\gamma_s)/(1-\bar{\psi}_{\mathrm{sb}}))mT_s)} \\ \times e^{-j2\pi f_c(\epsilon_s m^2 T_s^2/(1-\bar{\psi}_{\mathrm{sb}})+2\epsilon_s m T_s T_{\mathrm{cp}}/(1-\bar{\psi}_{\mathrm{sb}}))}. \end{aligned} \tag{29}$$

- *Delay steering vectors:* For even n, $\boldsymbol{b}_{\mathrm{b}}(\tau) \in \mathbb{C}^{N/2}$ with

$$\boldsymbol{b}_{\mathrm{b}}(\tau_b) = [1, e^{-j2\pi\Delta_f 2\tau_b}, \cdots e^{-j2\pi\Delta_f(N-2)\tau_b}]^{\mathsf{T}}. \tag{30}$$

and for odd n,

$$\begin{aligned} &\boldsymbol{b}_{\mathrm{s}}(\tau_s^{\mathrm{res}}) = \\ &[e^{-j2\pi\Delta_f\tau_s^{\mathrm{res}}}, e^{-j2\pi\Delta_f 3\tau_s^{\mathrm{res}}}, \cdots e^{-j2\pi\Delta_f(N-1)\tau_s^{\mathrm{res}}}]^{\mathsf{T}}. \end{aligned} \tag{31}$$

- *Modified Inverse Fourier matrices:* For even n, the matrix $\mathbf{F}_{m,\mathrm{b}}^{q}(\gamma_b,\epsilon_b) \in \mathbb{C}^{N\times N/2}$ is defined as

$$\begin{aligned} &[\mathbf{F}_{m,\mathrm{b}}^{q}(\gamma_b,\epsilon_b)]_{k,n} = \frac{1}{\sqrt{N}}\times \\ &e^{j2\pi(k/Nn(1-\gamma_b)-\epsilon_b k^2/N^2 nT_0-2\epsilon_b gk/NnT_0-2nm\epsilon_b k/NT_s)}, \end{aligned} \tag{32}$$

while for odd n

$$\begin{aligned} &[\mathbf{F}_{m,\mathrm{s}}^{q}(\gamma_s,\epsilon_s)]_{k,n} = \frac{1}{\sqrt{N}}\times \\ &e^{j2\pi(k/Nn(1-\gamma_s)-\epsilon_s k^2/N^2 nT_0-2\epsilon_s gk/NnT_0-2nm\epsilon_s k/NT_s)}, \end{aligned} \tag{33}$$

where $g = T_{\mathrm{cp}}/T_0$ is the cyclic-prefix overhead. The deviation of matrices $\mathbf{F}_{m,\mathrm{b}}^{q}(\gamma_b,\epsilon_b)$ and $\mathbf{F}_{m,\mathrm{s}}^{q}(\gamma_s,\epsilon_s)$ from the standard IDFT matrices produces loss of subcarrier orthogonality and hence an another source of ICI, but for typical parameter values this effect is much smaller than the ICI produced by (26)-(27).

- *Intersubcarrier Doppler effect:* For even n, $\mathbf{I}_{\mathrm{b}}^{q}(\gamma_b,\epsilon_b) \in \mathbb{C}^{N/2\times M}$, can be expressed as

$$\begin{aligned} &[\mathbf{I}_{\mathrm{b}}^{q}(\gamma_b,\epsilon_b)]_{n,m} = \\ &e^{-j2\pi(\gamma_b mn(g+1)+nm^2\epsilon_b(1+g)T_s+2mn\epsilon_b gT_s)}, \end{aligned} \tag{34}$$

while for odd n

$$\begin{aligned} &[\mathbf{I}_{\mathrm{s},m}^{q}(\gamma_s,\epsilon_s)]_{n,m} = \\ &e^{-j2\pi(\gamma_s mn(g+1)+nm^2\epsilon_s(1+g)T_s+2mn\epsilon_s gT_s)}. \end{aligned} \tag{35}$$

[4] The superscript 'res' stands for residual.

- *Intersubcarrier phase offset:* For even n, $\boldsymbol{q}_{\mathrm{b}}(\gamma_b) \in \mathbb{C}^{N/2}$, where
$$\boldsymbol{q}_{\mathrm{b}}(\gamma_b) = [1, e^{-j2\pi\gamma_b g 2}, \cdots, e^{-j2\pi\gamma_b g(N-2)}]^{\mathsf{T}}, \quad (36)$$
while for odd n
$$\boldsymbol{q}_{\mathrm{s}}(\gamma_s) = [e^{-j2\pi\gamma_s g}, \cdots, e^{-j2\pi\gamma_s g(N-1)}]^{\mathsf{T}}. \quad (37)$$
These offsets remain constant across M OFDM symbols.
- *Second-order crossed slow/fast-time Doppler effect*: Finally,
$$[\mathbf{H}_{\mathrm{b}}^{q}(\epsilon_b)]_{k,m} = e^{-j4\pi f_c \epsilon_b m T_s k T_0/N}, \quad (38)$$
$$[\mathbf{H}_{\mathrm{s}}^{q}(\epsilon_s)]_{k,m} = e^{-j4\pi f_c/(1-\bar{\psi}_{\mathrm{sb}})\epsilon_s m T_s k T_0/N}. \quad (39)$$

The received signal in (23) represents the full generative model, which is highly complex and challenging to handle. In the following subsection, four simplified models are proposed, arranged in decreasing order of complexity.

C. Simplified Models

In this subsection, four simplified models are introduced based on the true model (23), arranged in descending order of complexity. Table II summarizes which effects in the generative model are retained and which are omitted in the simplified models.

1) Model with constant channel (gain and AoD) and only first-order Doppler (CCFOD): This model is derived neglecting the Doppler rate and the second-order terms[5] in the effective Doppler shift and in the effective delay of the received signal, with the assumption that the channel gains and AoDs remain constant throughout the transmission of M OFDM symbols. Specifically, we set $\mu_{\mathrm{b}} = 0$ and $\mu_{\mathrm{s}} = 0$, which would change γ_b, γ_s, τ_{b} and $\tau_{\mathrm{s}}^{\mathrm{res}}$ in (14a) and (14c) as
$$\gamma_b = \psi_{\mathrm{b}}(1-\eta) + \eta, \quad (40a)$$
$$\gamma_s = \psi_{\mathrm{s}}(1-\eta) + \eta, \quad (40b)$$
$$\tau_{\mathrm{b}} = \tau_{\mathrm{b}}^{p} + \Delta_{t,0}(1-\eta)(1-\psi_{\mathrm{b}}), \quad (40c)$$
$$\tau_{\mathrm{s}} = \tau_{\mathrm{s}}^{p} + \Delta_{t,0}(1-\eta)(1-\psi_{\mathrm{s}}), \quad (40d)$$
while we set $\epsilon_{\mathrm{s}} = \epsilon_{\mathrm{b}} = 0$. Moreover, we consider $\alpha_{\mathrm{b}} = \alpha_{\mathrm{b}}(t = 0)$, $\alpha_{\mathrm{s}} = \alpha_{\mathrm{s}}(t = 0)$, $\boldsymbol{\theta} = \boldsymbol{\theta}(t = 0)$. Under these assumptions, the received signal simplifies to
$$\mathbf{Y} = \quad (41)$$
$$\sqrt{P_{\mathrm{b}}}\alpha_{\mathrm{b}}\mathbf{D}_{\mathrm{b}}(\gamma_b)\mathbf{F}_{\mathrm{b}}\big(\mathbf{I}_{\mathrm{b}}(\gamma_b) \odot (\boldsymbol{b}_{\mathrm{b}}(\tau_b)(\boldsymbol{z}(\boldsymbol{\theta}) \odot \mathbf{c}_{\mathrm{b}}(\gamma_b))^{\mathsf{T}})\big) +$$
$$\sqrt{P_{\mathrm{s}}}\alpha_{\mathrm{s}}\mathbf{D}_{\mathrm{s}}(\gamma_s)\mathbf{F}_{\mathrm{s}}(\gamma_{\mathrm{s}})\big(\mathbf{I}_{\mathrm{s}}(\gamma_s) \odot (\boldsymbol{b}_{\mathrm{s}}(\tau_s^{\mathrm{res}})\mathbf{c}_{\mathrm{s}}^{\mathsf{T}}(\gamma_s))\big) + \mathbf{N},$$
where the elements of the diagonal matrices $\mathbf{D}_{\mathrm{b}}(\gamma_b) = \mathbf{D}_{\mathrm{b}}^{q}(\gamma_b, \epsilon_b = 0)$, $\mathbf{D}_{\mathrm{s}}(\gamma_s) = \mathbf{D}_{\mathrm{s}}^{q}(\gamma_s, \epsilon_s = 0)$ are
$$[\mathbf{D}_{\mathrm{b}}(\gamma_b)]_{k,k} = e^{-j2\pi f_c \gamma_b T_0 k/N}, \quad (42)$$
$$[\mathbf{D}_{\mathrm{s}}(\gamma_s)]_{k,k} = e^{-j2\pi f_c(1-(1-\gamma_s)/(1-\bar{\psi}_{\mathrm{sb}}))T_0 k/N}, \quad (43)$$
while $\mathbf{F}_{\mathrm{b}} = \mathbf{F}_{\mathrm{b}}^{q}(\gamma_{\mathrm{b}}, \epsilon_{\mathrm{b}} = 0) \approx \mathbf{F}_{\mathrm{b}}^{q}(\gamma_{\mathrm{b}} = 0, \epsilon_{\mathrm{b}} = 0)$, $\mathbf{F}_{\mathrm{s}}(\gamma_{\mathrm{s}}) = \mathbf{F}_{\mathrm{s}}^{q}(\gamma_{\mathrm{s}}, \epsilon_{\mathrm{s}} = 0)$ are[6]
$$[\mathbf{F}_{\mathrm{b}}]_{k,n} = \frac{1}{\sqrt{N}} e^{j2\pi nk/N}, \text{ for even } n, \quad (44)$$
$$[\mathbf{F}_{\mathrm{s}}(\gamma_{\mathrm{s}})]_{k,n} = \frac{1}{\sqrt{N}} e^{j2\pi(1-\gamma_{\mathrm{s}})nk/N}, \text{ for odd } n. \quad (45)$$
Finally, $\mathbf{I}_{\mathrm{b}}(\gamma_b) = \mathbf{I}_{\mathrm{b}}^{q}(\gamma_b, \epsilon_b = 0)$, $\mathbf{I}_{\mathrm{s}}(\gamma_s) = \mathbf{I}_{\mathrm{s}}^{q}(\gamma_s, \epsilon_s = 0)$ are
$$[\mathbf{I}_{\mathrm{b},m}(\gamma_b)]_{n,m} = e^{-j2\pi\gamma_b mn(g+1)}, \text{ for even } n, \quad (46)$$
$$[\mathbf{I}_{\mathrm{s},m}(\gamma_s)]_{n,m} = e^{-j2\pi\gamma_s mn(g+1)}, \text{ for odd } n, \quad (47)$$
and $\mathbf{c}_{\mathrm{b}}(\gamma_b) = \mathbf{c}_{\mathrm{b}}^{q}(\gamma_b, \epsilon_b = 0)$, $\mathbf{c}_{\mathrm{s}}(\gamma_s) = \mathbf{c}_{\mathrm{s}}^{q}(\gamma_s, \epsilon_s = 0)$ are
$$[\mathbf{c}_{\mathrm{b}}(\gamma_b)]_m = e^{-j2\pi f_c \gamma_b m T_s}, \quad (48)$$
$$[\mathbf{c}_{\mathrm{s}}(\gamma_s)]_m = e^{-j2\pi f_c((1-(1-\gamma_s)/(1-\bar{\psi}_{\mathrm{sb}}))mT_s)}, \quad (49)$$
and $[\boldsymbol{z}(\boldsymbol{\theta})]_m = \boldsymbol{w}'^{\mathsf{T}}(t' = mT_s + T_{\mathrm{cp}})\boldsymbol{a}(\boldsymbol{\theta})$ and $\boldsymbol{q}_{\mathrm{b}}(\gamma_{\mathrm{b}})$ and $\boldsymbol{q}_{\mathrm{s}}(\gamma_{\mathrm{s}})$ are neglected[7]. Table. III summarizes the transformation from the generative model to the CCFOD model.

2) Model without ICI (CCFODnoICI): As the next step towards simplifying (23), we neglect ICI and Doppler effect on subcarriers over fast time (related to (45)) as well. Therefore the received signal can be modeled as
$$\mathbf{Y} = \sqrt{P_{\mathrm{b}}}\alpha_{\mathrm{b}}\mathbf{F}_{\mathrm{b}}\big(\mathbf{I}_{\mathrm{b}}(\gamma_b) \odot (\boldsymbol{b}_{\mathrm{b}}(\tau_b)(\boldsymbol{z}(\boldsymbol{\theta}) \odot \mathbf{c}_{\mathrm{b}}(\gamma_b))^{\mathsf{T}})\big)$$
$$+ \sqrt{P_{\mathrm{s}}}\alpha_{\mathrm{s}}\mathbf{F}_{\mathrm{s}}\big(\mathbf{I}_{\mathrm{s}}(\gamma_s) \odot (\boldsymbol{b}_{\mathrm{s}}(\tau_s^{\mathrm{res}})\mathbf{c}_{\mathrm{s}}^{\mathsf{T}}(\gamma_s))\big) + \mathbf{N}. \quad (50)$$
Here, $\mathbf{F}_{\mathrm{s}} = \mathbf{F}_{\mathrm{s}}^{q}(\gamma_s = 0, \epsilon_s = 0)$.

3) Model with only Slow Doppler (SlowD): To further simplify the received signal, we neglect the intersubcarrier Doppler effect as well, leading to
$$\mathbf{Y} = \sqrt{P_{\mathrm{b}}}\alpha_{\mathrm{b}}\mathbf{F}_{\mathrm{b}}(\boldsymbol{b}_{\mathrm{b}}(\tau_b)(\boldsymbol{z}(\boldsymbol{\theta}) \odot \mathbf{c}_{\mathrm{b}}(\gamma_b))^{\mathsf{T}})$$
$$+ \sqrt{P_{\mathrm{s}}}\alpha_{\mathrm{s}}\mathbf{F}_{\mathrm{s}}(\boldsymbol{b}_{\mathrm{s}}(\tau_s^{\mathrm{res}})\mathbf{c}_{\mathrm{s}}^{\mathsf{T}}(\gamma_s)) + \mathbf{N}, \quad (51)$$
in which only the slow-time Doppler effect is present, meaning that the phase changes for every OFDM symbol and is constant throughout N subcarriers in each OFDM symbol. This model is common in the OFDM integrated sensing and communication (ISAC) literature [32].

4) Communication Coherence Interval Model (Comm): Finally, we derive the simplest model, where mobility is assumed but the CFO and Doppler effects are considered negligible due to their minimal impact over the short observation period. In this model, these effects are treated as a fixed phase over the entire frame, which can be absorbed into the channel gain. Consequently, neither slow nor fast time Doppler nor CFO effects are accounted for, and no phase rotation over time is observed. Under these assumptions, the received signal can be expressed as follows:
$$\mathbf{Y} = \sqrt{P_{\mathrm{b}}}\alpha_{\mathrm{b}}\mathbf{F}_{\mathrm{b}}(\boldsymbol{b}_{\mathrm{b}}(\tau_b)\boldsymbol{z}^{\mathsf{T}}(\boldsymbol{\theta})) + \sqrt{P_{\mathrm{s}}}\alpha_{\mathrm{s}}\mathbf{F}_{\mathrm{s}}(\boldsymbol{b}_{\mathrm{s}}(\tau_s^{\mathrm{res}})\mathbf{1}_M^{\mathsf{T}}) + \mathbf{N}. \quad (52)$$
This model is common in the communication literature [33] and also the positioning literature under low mobility [34].

IV. Estimation Algorithms

In this section, we present the maximum likelihood (ML) estimation algorithms corresponding to the proposed simplified models in Section III-C, starting with the simplest model and progressing to more complex ones.

A. Channel Parameter Estimation

1) Model Comm: The channel-domain parameter vector is
$$\boldsymbol{\chi}_{\mathrm{ch}}^{a} = [\alpha_{\mathrm{R,b}}, \alpha_{\mathrm{I,b}}, \alpha_{\mathrm{R,s}}, \alpha_{\mathrm{I,s}}, \tau_b, \tau_s^{\mathrm{res}}, \boldsymbol{\theta}^{\mathsf{T}}]^{\mathsf{T}} \in \mathbb{R}^8. \quad (53)$$

[5] By "second-order terms," we refer to the components that depend on ϵ_{b} or ϵ_{s}.

[6] Since γ_{b} is much smaller than γ_{s}, and Doppler precompensation in our setup affects only the carrier frequency, we can approximate $\mathbf{F}_{\mathrm{b}}^{q}(\gamma_{\mathrm{b}}, \epsilon_{\mathrm{b}} = 0) \approx \mathbf{F}_{\mathrm{b}}^{q}(\gamma_{\mathrm{b}} = 0, \epsilon_{\mathrm{b}} = 0) = \mathbf{F}_{\mathrm{b}}$, effectively reducing this matrix to the IDFT matrix. If Doppler precompensation was applied at both the carrier frequency and the subcarrier levels, a value of $\gamma_{\mathrm{s}} = 0$ could be used in $\mathbf{F}_{\mathrm{s}}^{q}(\gamma_{\mathrm{s}}, \epsilon_{\mathrm{s}} = 0)$, which would similarly reduce to the IDFT matrix.

[7] The vectors $\boldsymbol{q}_{\mathrm{b}}(\gamma_{\mathrm{b}})$ and $\boldsymbol{q}_{\mathrm{s}}(\gamma_{\mathrm{s}})$ induce only very small per-subcarrier phase shifts. Since γ_i are between 10^{-6} and 10^{-4} in our setting, these shifts are $\ll 10^{-3}$ rad and therefore negligible.

TABLE II
RELATION BETWEEN GENERATIVE MODEL AND SIMPLIFIED MODELS

Feature	Generative	CCFOD	CCFODnoICI	SlowD	Comm
Satellite Doppler rate (μ_s)	✓	×	×	×	×
BS Doppler rate (μ_b)	✓	×	×	×	×
Time variation (α_b, α_s, $\boldsymbol{\theta}_b$)	✓	×	×	×	×
ICI ($\mathbf{D}_\mathrm{s}, \mathbf{D}_\mathrm{b}$)	✓	✓	×	×	×
Inter-subcarrier Doppler effect ($\mathbf{I}_\mathrm{s}, \mathbf{I}_\mathrm{b}$)	✓	✓	✓	×	×
Slow-time Doppler ($\mathbf{c}_\mathrm{b}, \mathbf{c}_\mathrm{s}$)	✓	✓	✓	✓	×

TABLE III
TRANSFORMATION OF MATRICES AND VECTORS FROM THE GENERATIVE MODEL (24)–(25) TO THE CCFOD MODEL (41).

Term	Gen. Model	CCFOD Model	Reason for Simplification
Time-varying gains	$\mathbf{A}_b$, $\mathbf{A}_s$	α_b, α_s (constants)	Channel variation across m symbols neglected.
Time-varying beamformer term	$\mathbf{Z}$	$\mathbf{z}(\theta)$	AoD assumed constant; time-varying steering only over OFDM symbols.
ICI matrices	$\mathbf{D}_b^q(\gamma_b, \epsilon_b)$, $\mathbf{D}_s^q(\gamma_s, \epsilon_s)$	$\mathbf{D}_b(\gamma_b)$, $\mathbf{D}_s(\gamma_s)$	Second-order Doppler terms removed; only first-order Doppler retained.
Modified Fourier matrices	$\mathbf{F}_{m,b}^q(\gamma_b, \epsilon_b)$, $\mathbf{F}_{m,s}^q(\gamma_s, \epsilon_s)$	$\mathbf{F}_b$, $\mathbf{F}_s(\gamma_s)$	Second-order Doppler terms removed; BS reduces to IDFT, satellite retains $(1-\gamma_s)$ scaling.
Intersubcarrier Doppler matrices	$\mathbf{I}_b^q(\gamma_b, \epsilon_b)$, $\mathbf{I}_s^q(\gamma_s, \epsilon_s)$	$\mathbf{I}_b(\gamma_b)$, $\mathbf{I}_s(\gamma_s)$	Doppler rate (ϵ_b, ϵ_s) eliminated.
Slow-time Doppler vectors	$\mathbf{c}_b^q(\gamma_b, \epsilon_b)$, $\mathbf{c}_s^q(\gamma_s, \epsilon_s)$	$\mathbf{c}_b(\gamma_b)$, $\mathbf{c}_s(\gamma_s)$	Only first-order slow-time Doppler retained.
Delay steering vectors	$\mathbf{b}_b(\tau_b)$, $\mathbf{b}_s(\tau_s^{\mathrm{res}})$	unchanged	Depend only on delays and first-order parameters.
Intersubcarrier phase vectors	$\mathbf{q}_b(\gamma_b)$, $\mathbf{q}_s(\gamma_s)$	neglected	Phase shifts are $\ll 10^{-3}$ rad for system parameters; negligible impact.
Second-order mixed Doppler	$\mathbf{H}_b^q(\epsilon_b)$, $\mathbf{H}_s^q(\epsilon_s)$	removed	All second-order Doppler components suppressed.

Since the satellite-UE and BS-UE paths do not share any common unknown parameters, each path can be analyzed independently. Leveraging the structure of model Comm, along with the orthogonal subcarriers employed by the BS and the satellite, the contributions from the BS and satellite can be separated as follows:

$$\tilde{\mathbf{Y}}_\mathrm{b} = \mathbf{F}_\mathrm{b}^\mathsf{H}\mathbf{Y}, \tag{54}$$

$$\tilde{\mathbf{Y}}_\mathrm{s} = \mathbf{F}_\mathrm{s}^\mathsf{H}\mathbf{Y}. \tag{55}$$

To estimate τ_s^{res}, the following problem needs to be solved:

$$[\hat{\tau}_s^{\mathrm{res}}, \hat{\alpha}_\mathrm{s}] = \arg\min_{\tau,\alpha_\mathrm{s}} \|\tilde{\mathbf{Y}}_\mathrm{s} - \alpha_\mathrm{s}\sqrt{P_\mathrm{s}}\boldsymbol{b}_\mathrm{s}(\tau)\mathbf{1}_M^\mathsf{T}\|^2, \tag{56}$$

which results in

$$\hat{\tau}_s^{\mathrm{res}} = \arg\min_{\tau} \|\tilde{\mathbf{Y}}_\mathrm{s} - \hat{\alpha}_\mathrm{s}(\tau)\sqrt{P_\mathrm{s}}\boldsymbol{b}_\mathrm{s}(\tau)\mathbf{1}_M^\mathsf{T}\|^2, \tag{57}$$

where

$$\hat{\alpha}_\mathrm{s}(\tau) = \frac{\|\tilde{\mathbf{Y}}_\mathrm{s}\mathbf{1}_M\boldsymbol{b}_\mathrm{s}^\mathsf{H}(\tau)\|^2}{\sqrt{P_s}\|\boldsymbol{b}_\mathrm{s}(\tau)\mathbf{1}_M^\mathsf{T}\|^2} = \frac{\|\tilde{\mathbf{Y}}_\mathrm{s}\mathbf{1}_M\boldsymbol{b}_\mathrm{s}^\mathsf{H}(\tau)\|^2}{\sqrt{P_s}MN/2}. \tag{58}$$

It follows with (57) that

$$\hat{\tau}_s^{\mathrm{res}} = \arg\max_{\tau} \left|\boldsymbol{b}_\mathrm{s}^\mathsf{H}(\tau)\tilde{\mathbf{Y}}_\mathrm{s}\mathbf{1}_M\right|. \tag{59}$$

The problem is initially solved by performing a 1D grid search, which can then be refined using a 1D quasi-Newton algorithm to obtain more accurate estimates of τ_s^{res}.

To estimate τ_b and $\boldsymbol{\theta}$, the following problem needs to be solved:

$$[\hat{\tau}_b, \hat{\boldsymbol{\theta}}^\mathsf{T}, \hat{\alpha}_\mathrm{b}] = \arg\min_{\tau,\boldsymbol{\theta},\alpha_\mathrm{b}} \|\tilde{\mathbf{Y}}_\mathrm{b} - \alpha_\mathrm{b}\sqrt{P_\mathrm{b}}\boldsymbol{b}_\mathrm{b}(\tau)\boldsymbol{z}^\mathsf{T}(\boldsymbol{\theta})\|^2. \tag{60}$$

which results in

$$[\hat{\tau}_b, \hat{\boldsymbol{\theta}}^\mathsf{T}] = \arg\min_{\tau,\boldsymbol{\theta}} \|\tilde{\mathbf{Y}}_\mathrm{b} - \hat{\alpha}_\mathrm{b}(\tau,\boldsymbol{\theta})\sqrt{P_\mathrm{b}}\boldsymbol{b}_\mathrm{b}(\tau)\boldsymbol{z}^\mathsf{T}(\boldsymbol{\theta})\|^2. \tag{61}$$

where

$$\hat{\alpha}_\mathrm{b}(\tau,\boldsymbol{\theta}) = \frac{\|\tilde{\mathbf{Y}}_\mathrm{b}(\boldsymbol{z}(\boldsymbol{\theta})^*\boldsymbol{b}_\mathrm{b}^\mathsf{H}(\tau))\|^2}{\sqrt{P_\mathrm{b}}\|\boldsymbol{b}_\mathrm{b}(\tau)\boldsymbol{z}^\mathsf{T}(\boldsymbol{\theta})\|^2}. \tag{62}$$

The estimation problem (60) can be solved using a separate 1D and 2D grid search, where the initial search is to estimate the delay

$$\hat{\tau}_b = \arg\max_{\tau} \left|\boldsymbol{b}_\mathrm{b}^\mathsf{H}(\tau)\tilde{\mathbf{Y}}_\mathrm{b}\mathbf{1}_M\right|, \tag{63}$$

followed by 2D AoD search

$$\hat{\boldsymbol{\theta}} = \arg\max_{\boldsymbol{\theta}} \left|\boldsymbol{b}_\mathrm{b}^\mathsf{H}(\hat{\tau}_b)\tilde{\mathbf{Y}}_\mathrm{b}\boldsymbol{z}^*(\boldsymbol{\theta})\right|. \tag{64}$$

We can refine our estimates using (60) by performing the quasi-Newton algorithm.

2) Model SlowD: In model SlowD, the channel-domain parameter vector is

$$\boldsymbol{\chi}_{\mathrm{ch}}^b = [\boldsymbol{\chi}_{\mathrm{ch}}^{a\,\mathsf{T}}, \gamma_b, \gamma_s]^\mathsf{T} \in \mathbb{R}^{10}. \tag{65}$$

Similar to model Comm, the BS-UE and satellite-UE paths can be separated due to the use of orthogonal subcarriers using (54) and (55). To estimate τ_s^{res} and γ_s, the following problem needs to be solved:

$$[\hat{\tau}_s^{\mathrm{res}}, \hat{\gamma}_s] = \arg\min_{\tau,\gamma} \|\tilde{\mathbf{Y}}_\mathrm{s} - \hat{\alpha}_\mathrm{s}(\tau,\gamma)\sqrt{P_\mathrm{s}}\boldsymbol{b}_\mathrm{s}(\tau)\mathbf{c}_\mathrm{s}(\gamma)^\mathsf{T}\|^2, \tag{66}$$

where

$$\hat{\alpha}_s(\tau,\gamma) = \frac{\|\tilde{\mathbf{Y}}_\mathrm{s}(\mathbf{c}_\mathrm{s}^*(\gamma)\boldsymbol{b}_\mathrm{s}^\mathsf{H}(\tau))\|^2}{\sqrt{P_s}\|\boldsymbol{b}_\mathrm{s}(\tau)\mathbf{c}_\mathrm{s}(\gamma)^\mathsf{T}\|^2}. \tag{67}$$

Since τ_s^{res} is related to the subcarriers and γ_s is associated with the slow-time samples, these parameters can be estimated independently using separate grid searches. To estimate τ_s^{res}, we utilize (59). Subsequently, this result can be used to estimate γ_s accordingly:

$$\hat{\gamma}_s = \arg\max_{\gamma} \left|\boldsymbol{b}_\mathrm{s}^\mathsf{H}(\hat{\tau}_s^{\mathrm{res}})\tilde{\mathbf{Y}}_\mathrm{s}\mathbf{c}_\mathrm{s}^*(\gamma)\right|. \tag{68}$$

For estimating parameters in the BS-UE path, the following problem needs to be solved:

$$[\hat{\tau}_b, \gamma_b, \hat{\boldsymbol{\theta}}^\mathsf{T}] = \arg\min_{\tau,\gamma,\boldsymbol{\theta}} \|\tilde{\mathbf{Y}}_\mathrm{b} - \hat{\alpha}_\mathrm{b}(\tau,\gamma,\boldsymbol{\theta})\sqrt{P_\mathrm{b}}(\boldsymbol{b}_\mathrm{b}(\tau)(\boldsymbol{z}(\boldsymbol{\theta}) \odot \mathbf{c}_\mathrm{b}(\gamma))^\mathsf{T})\|^2, \tag{69}$$

where

$$\hat{\alpha}_{\mathrm{b}}(\tau,\gamma,\boldsymbol{\theta})=\frac{\|\tilde{\mathbf{Y}}_{\mathrm{b}}((\boldsymbol{z}^{*}(\boldsymbol{\theta})\odot\mathbf{c}_{\mathrm{b}}^{*}(\gamma))\boldsymbol{b}_{\mathrm{b}}^{\mathsf{H}}(\tau))\|^{2}}{\sqrt{P_{\mathrm{b}}}\|\boldsymbol{b}_{\mathrm{b}}(\tau)(\boldsymbol{z}(\boldsymbol{\theta})\odot\mathbf{c}_{\mathrm{b}}(\gamma))^{\mathsf{T}}\|^{2}}. \tag{70}$$

It can be observed that while τ_b is associated with subcarrier dimension, both $\boldsymbol{\theta}$ and γ_b vary over slow-time domain. This variation leads to angle-Doppler coupling in the slow-time domain, and to tackle the estimation problem, a 1D grid search followed by a 3D grid search (2D angle + Doppler) is required in the basic approach. The 1D grid search is used to estimate τ_b, and the subsequent 3D grid search jointly estimates $\boldsymbol{\theta}$ and γ_b. This complexity can be reduced by designing the beamforming matrix with repetitive angles over a subset of the observations, such as the first P samples, similar to the solution in [35]. For this subset, the beamforming matrix remains fixed, meaning that no angle information is embedded in these observations. As a result, Doppler can be estimated independently of the angles. Once γ_b is estimated from this subset, the full set of observations can then be used to estimate the angles $\boldsymbol{\theta}$, effectively decoupling the 3D grid search into a 1D Doppler search and a 2D angle search. Therefore, an estimate for τ_b is obtained using (63). Furthermore, an estimate of γ_b can be found by leveraging the first P slow-time samples of $\tilde{\mathbf{Y}}_{\mathrm{b}}$:

$$\hat{\gamma}_b=\arg\max_{\gamma}\left|\boldsymbol{b}_{\mathrm{b}}^{\mathsf{H}}(\hat{\tau}_b)[\tilde{\mathbf{Y}}_{\mathrm{b}}]_{(:,1:P)}[\mathbf{c}_{\mathrm{b}}^{*}(\gamma)]_{(1:P)}\right|, \tag{71}$$

and then the full set of observations can be utilized to estimate $\boldsymbol{\theta}$ as

$$\hat{\boldsymbol{\theta}}=\arg\max_{\boldsymbol{\theta}}\left|\boldsymbol{b}_{\mathrm{b}}^{\mathsf{H}}(\hat{\tau}_b)\tilde{\mathbf{Y}}_{\mathrm{b}}(\mathbf{c}_{\mathrm{b}}^{*}(\hat{\gamma}_b)\odot\boldsymbol{z}^{*}(\boldsymbol{\theta}))\right|. \tag{72}$$

Finally, by performing the quasi-Newton algorithm we can refine our estimates.

3) Model CCFODnoICI: The channel-domain parameter vector in model CCFODnoICI is identical to that in model SlowD, as $\boldsymbol{\chi}_{\mathrm{ch}}^{b}$. The process begins by separating the BS-UE and satellite-UE contributions, using (54) and (55). To estimate τ_s^{res} and γ_s, the following problem needs to be solved:

$$[\hat{\tau}_s^{\mathrm{res}},\hat{\gamma}_s]=\arg\min_{\tau,\gamma}\|\tilde{\mathbf{Y}}_{\mathrm{s}}-\hat{\alpha}_{\mathrm{s}}(\tau,\gamma)\sqrt{P_{\mathrm{s}}}\mathbf{I}_{\mathrm{s}}(\gamma)\odot(\boldsymbol{b}_{\mathrm{s}}(\tau)\mathbf{c}_{\mathrm{s}}(\gamma)^{\mathsf{T}})\|^{2}, \tag{73}$$

where

$$\hat{\alpha}_{s}(\tau,\gamma)=\frac{\|\tilde{\mathbf{Y}}_{\mathrm{s}}(\mathbf{I}_{\mathrm{s}}^{\mathsf{H}}(\gamma)\odot\mathbf{c}_{\mathrm{s}}^{*}(\gamma)\boldsymbol{b}_{\mathrm{s}}^{\mathsf{H}}(\tau))\|^{2}}{\sqrt{P_s}\|\mathbf{I}_{\mathrm{s}}^{\mathsf{H}}(\gamma)\odot(\boldsymbol{b}_{\mathrm{s}}(\tau)\mathbf{c}_{\mathrm{s}}(\gamma)^{\mathsf{T}})\|^{2}}. \tag{74}$$

The primary distinction between model CCFODnoICI and model SlowD lies in the inclusion of the intersubcarrier Doppler effect ($\mathbf{I}_{\mathrm{b}}(\gamma_b)$ and $\mathbf{I}_{\mathrm{s}}(\gamma_s)$). Given that a significant portion of γ_s is already known from $\bar{\psi}_{\mathrm{sb}}$, this prior knowledge can be leveraged to partially mitigate the intersubcarrier Doppler effect in the satellite-UE contribution. This can facilitate satellite-UE parameter estimation. We can estimate $\gamma_s$as

$$\hat{\gamma}_s=\arg\max_{\gamma}\left|\mathbf{1}_{N/2}^{\mathsf{T}}(\tilde{\mathbf{Y}}_{\mathrm{s}}\odot\mathbf{I}_{\mathrm{s}}^{*}(\bar{\psi}_{\mathrm{sb}}))\mathbf{c}_{\mathrm{s}}^{*}(\gamma)\right| \tag{75}$$

and estimate τ_s^{res}as follows

$$\hat{\tau}_s^{\mathrm{res}}=\arg\max_{\tau}\left|\boldsymbol{b}_{\mathrm{s}}^{\mathsf{H}}(\tau)(\tilde{\mathbf{Y}}_{\mathrm{s}}\odot\mathbf{I}_{\mathrm{s}}^{*}(\hat{\gamma}_s))\mathbf{c}_{\mathrm{s}}^{*}(\hat{\gamma}_s)\right|. \tag{76}$$

The term $\mathbf{I}_{\mathrm{s}}(\gamma_s)$, initially approximated using a proxy to simplify the grid search, is then fully incorporated during the refinement step to improve the estimation accuracy.

To estimate τ_b, γ_b and $\boldsymbol{\theta}$, the following problem needs to be solved:

$$[\hat{\tau}_b,\gamma_b,\hat{\boldsymbol{\theta}}^{\mathsf{T}}]=\arg\min_{\tau,\gamma,\boldsymbol{\theta}}\|\tilde{\mathbf{Y}}_{\mathrm{b}}-\hat{\alpha}_{\mathrm{b}}(\tau,\gamma,\boldsymbol{\theta})\sqrt{P_{\mathrm{b}}}\mathbf{I}_{\mathrm{b}}(\gamma)\odot(\boldsymbol{b}_{\mathrm{b}}(\tau)(\boldsymbol{z}(\boldsymbol{\theta})\odot\mathbf{c}_{\mathrm{b}}(\gamma))^{\mathsf{T}})\|^{2}, \tag{77}$$

where

$$\hat{\alpha}_{\mathrm{b}}(\tau,\gamma,\boldsymbol{\theta})=\frac{\|\tilde{\mathbf{Y}}_{\mathrm{b}}(\mathbf{I}_{\mathrm{b}}^{\mathsf{H}}(\gamma)\odot(\boldsymbol{z}^{*}(\boldsymbol{\theta})\odot\mathbf{c}_{\mathrm{b}}^{*}(\gamma))\boldsymbol{b}_{\mathrm{b}}^{\mathsf{H}}(\tau))\|^{2}}{\sqrt{P_{\mathrm{b}}}\|\mathbf{I}_{\mathrm{b}}(\gamma)\odot(\boldsymbol{b}_{\mathrm{b}}(\tau)(\boldsymbol{z}(\boldsymbol{\theta})\odot\mathbf{c}_{\mathrm{b}}(\gamma))^{\mathsf{T}})\|^{2}}. \tag{78}$$

Coarse estimates are first obtained by neglecting the term $\mathbf{I}_{\mathrm{b}}(\gamma_b)$ to simplify the initial grid search, using (63), (71), and (72). These estimates are then refined by reintroducing $\mathbf{I}_{\mathrm{b}}(\gamma_b)$ and solving the full objective in (77).

4) Model CCFOD: The channel-domain parameter vector in model CCFOD is the same as the one in model SlowD and model CCFODnoICI. The key difference between model CCFOD and other simplified models is that due to the existence of ICI represented by $\mathbf{D}_{\mathrm{b}}(\gamma_b)$ and $\mathbf{D}_{\mathrm{s}}(\gamma_s)$, there may be leakage between the BS-UE and satellite-UE paths. As a result, the two paths can only be partially separated using simple processing as outlined in (54) and (55). To estimate γ_b, τ_b and $\boldsymbol{\theta}$, we need to solve

$$[\hat{\tau}_b,\gamma_b,\hat{\boldsymbol{\theta}}^{\mathsf{T}}]=\arg\min_{\tau,\gamma,\boldsymbol{\theta}}\|\mathbf{F}_{\mathrm{b}}^{\mathsf{H}}\mathbf{D}_{\mathrm{b}}^{\mathsf{H}}(\gamma)\mathbf{Y}-\hat{\alpha}_{\mathrm{b}}(\tau,\gamma,\boldsymbol{\theta})\sqrt{P_{\mathrm{b}}}\mathbf{I}_{\mathrm{b}}(\gamma)\odot(\boldsymbol{b}_{\mathrm{b}}(\tau)(\boldsymbol{z}(\boldsymbol{\theta})\odot\mathbf{c}_{\mathrm{b}}(\gamma))^{\mathsf{T}})\|^{2}, \tag{79}$$

where

$$\hat{\alpha}_{\mathrm{b}}(\tau,\gamma,\boldsymbol{\theta})=\frac{\|\tilde{\mathbf{Y}}_{\mathrm{b}}(\mathbf{I}_{\mathrm{b}}^{\mathsf{H}}(\gamma)\odot(\boldsymbol{z}^{*}(\boldsymbol{\theta})\odot\mathbf{c}_{\mathrm{b}}^{*}(\gamma))\boldsymbol{b}_{\mathrm{b}}^{\mathsf{H}}(\tau))\|^{2}}{\sqrt{P_{\mathrm{b}}}\|\mathbf{I}_{\mathrm{b}}(\gamma)\odot(\boldsymbol{b}_{\mathrm{b}}(\tau)(\boldsymbol{z}(\boldsymbol{\theta})\odot\mathbf{c}_{\mathrm{b}}(\gamma))^{\mathsf{T}})\|^{2}}. \tag{80}$$

To estimate γ_s and τ_s^{res} we proceed by

$$[\hat{\tau}_s^{\mathrm{res}},\hat{\gamma}_s]=\arg\min_{\tau,\gamma}\|\mathbf{F}_{\mathrm{s}}^{\mathsf{H}}\mathbf{D}_{\mathrm{s}}^{\mathsf{H}}(\gamma)\mathbf{Y}-\hat{\alpha}_{\mathrm{s}}(\tau,\gamma)\sqrt{P_{\mathrm{s}}}\mathbf{I}_{\mathrm{s}}(\gamma)\odot(\boldsymbol{b}_{\mathrm{s}}(\tau)\mathbf{c}_{\mathrm{s}}(\gamma)^{\mathsf{T}})\|^{2}, \tag{81}$$

where

$$\hat{\alpha}_{s}(\tau,\gamma)=\frac{\|\tilde{\mathbf{Y}}_{\mathrm{s}}(\mathbf{I}_{\mathrm{s}}^{\mathsf{H}}(\gamma)\odot\mathbf{c}_{\mathrm{s}}^{*}(\gamma)\boldsymbol{b}_{\mathrm{s}}^{\mathsf{H}}(\tau))\|^{2}}{\sqrt{P_s}\|\mathbf{I}_{\mathrm{s}}^{\mathsf{H}}(\gamma)\odot(\boldsymbol{b}_{\mathrm{s}}(\tau)\mathbf{c}_{\mathrm{s}}(\gamma)^{\mathsf{T}})\|^{2}}. \tag{82}$$

To tackle (79), the presence of $\mathbf{D}_{\mathrm{b}}(\gamma_b)$ and $\mathbf{I}_{\mathrm{b}}(\gamma_b)$ is temporarily neglected. Therefore, we apply (54) and (55) to partially separate two paths, and then leverage (63), (71) and (72) similar to the procedures model SlowD and model CCFODnoICI to estimate γ_b, τ_b and $\boldsymbol{\theta}$. These estimates are then refined by incorporating $\mathbf{D}_{\mathrm{b}}(\gamma_b)$ and $\mathbf{I}_{\mathrm{b}}(\gamma_b)$ using (79), enabling the full reconstruction of the BS path $\tilde{\mathbf{Y}}_{\mathrm{b}}$.

In the next step, we remove the reconstructed BS path from $\mathbf{Y}$ to facilitate separating the satellite-UE contribution. Now to estimate the satellite-UE related parameters (τ_s^{res} and γ_s), similar to the estimation algorithm in model CCFODnoICI, we use $\bar{\psi}_{\mathrm{sb}}$ to eliminate the effect of $\mathbf{D}_{\mathrm{s}}$ and $\mathbf{I}_{\mathrm{s}}$ partly, then we estimate γ_s and τ_s^{res} as

$$\hat{\gamma}_s=\arg\max_{\gamma}\left|\mathbf{1}_{N/2}^{\mathsf{T}}(\mathbf{F}_{\mathrm{s}}^{\mathsf{H}}\mathbf{D}_{\mathrm{s}}^{\mathsf{H}}(\bar{\psi}_{\mathrm{sb}})(\mathbf{Y}-\tilde{\mathbf{Y}}_{\mathrm{b}})\odot\mathbf{I}_{\mathrm{s}}^{*}(\bar{\psi}_{\mathrm{sb}}))\mathbf{c}_{\mathrm{s}}^{*}(\gamma)\right|, \tag{83}$$

$$\hat{\tau}_s^{\mathrm{res}}=\arg\max_{\tau}\left|\boldsymbol{b}_{\mathrm{s}}^{\mathsf{H}}(\tau)(\mathbf{F}_{\mathrm{s}}^{\mathsf{H}}\mathbf{D}_{\mathrm{s}}^{\mathsf{H}}(\hat{\gamma}_s)(\mathbf{Y}-\tilde{\mathbf{Y}}_{\mathrm{b}})\odot\mathbf{I}_{\mathrm{s}}^{*}(\hat{\gamma}_s))\mathbf{c}_{\mathrm{s}}^{*}(\hat{\gamma}_s)\right|. \tag{84}$$

Remark 1. *All the estimators presented in this section can be improved by considering the first two peaks in the first grid*

search for each path (e.g., (59) *and* (63) *in model Comm) to account for potential leakage from the other path when using data from the true model.*

Remark 2. *According to* (49)*, the maximum unambiguous interval for estimating γ_s is $(1-\bar{\psi}_{sb})/(f_c T_s)$. However, due to the velocities of LEO satellites and the Earth's rotation considered in γ_s, this value may exceed the maximum range in certain scenarios. To address this issue, the known parameter $\bar{\psi}_{sb}$ is used to determine the integer part corresponding to the unambiguous range within the actual Doppler γ_s. Given that the UE's velocity is significantly smaller than the LEO satellite and Earth's velocities, and that the UE is in close proximity to the BS, the integer factors for $\bar{\psi}_{sb}$ and γ_s are expected to be identical. Consequently, only the residual Doppler needs to be estimated, after which the known integer factor can be applied to accurately retrieve γ_s.*

B. Location, Clock Offset, Velocity and CFO Estimation

All models provide two TOA measurements and a single AOD tuple, which can be used to position the UE and estimate its clock offset [36]. Models SlowD, CCFODnoICI, and CCFOD, however, also provide two additional Doppler measurements, which can be utilized to estimate the UE's radial velocity and CFO.

As for estimating $\boldsymbol{p}_0$ and $\Delta_{t,0}$, it is possible to neglect the factors $(1-\eta)(1-\psi_{\mathrm{b}})$ and $(1-\eta)(1-\psi_{\mathrm{s}})$ in (40c) and (40d) due to their small nominal values for simplicity.[8] Moreover, we can write the expression for the line passing the BS with AoD $\hat{\boldsymbol{\theta}}$ according to $\boldsymbol{p}_0(\beta) = \boldsymbol{p}_{\mathrm{b}} + \beta\hat{\boldsymbol{u}}$, where $\hat{\boldsymbol{u}} = \boldsymbol{u}(\hat{\boldsymbol{\theta}})$. Therefore we can find $\hat{\boldsymbol{p}}_0$ using $\hat{\boldsymbol{p}}_0 = \boldsymbol{p}_0(\hat{\beta})$ where

$$\hat{\beta} = \arg\min_{\beta} \left| \frac{\|\boldsymbol{p}_0(\beta) - \boldsymbol{p}_{\mathrm{b}}\|}{c} - \frac{\|\boldsymbol{p}_0(\beta) - \boldsymbol{p}_{\mathrm{s}}\|}{c} - (\hat{\tau}_b - \hat{\tau}_s^{\mathrm{res}} - \bar{\tau}_{\mathrm{sb}}) \right|, \quad (85)$$

and $\hat{\Delta}_{t,0}$ can be found as a weighted combination of residual delays, where each residual represents the difference between the measured delay and the expected geometric delay from the estimated position:

$$\hat{\Delta}_{t,0} = \frac{1}{D+1}\left(\hat{\tau}_b - \frac{\|\boldsymbol{p}_b - \hat{\boldsymbol{p}}_0\|}{c}\right) + \frac{D}{D+1}\left(\hat{\tau}_s^{\mathrm{res}} + \bar{\tau}_{bs} - \frac{\|\boldsymbol{p}_s - \hat{\boldsymbol{p}}_0\|}{c}\right), \quad (86)$$

where $D = \|\hat{\boldsymbol{p}}_0 - \boldsymbol{p}_b\|/\|\hat{\boldsymbol{p}}_0 - \boldsymbol{p}_s\|$. This heuristic weighted averaging approach puts more trust in the delay estimate from the transmitter that is closer to the user, which in our case, is the BS.

As for estimating $\|\boldsymbol{v}\|$ and η, due to the structure of model Comm with neglecting any phase change in the transmission of M OFDM symbols, it is not possible to estimate $\|\boldsymbol{v}\|$ and η. But in models SlowD, CCFODnoICI and CCFOD, it holds that $\gamma_b = \eta + (1-\eta)\psi_{\mathrm{b}}$ and $\gamma_s = \eta + (1-\eta)\psi_{\mathrm{s}}$, where

$$\psi_{\mathrm{b}} = \frac{\|\boldsymbol{v}\|(\boldsymbol{p}_0 - \boldsymbol{p}_{\mathrm{b}})^{\mathsf{T}}\vec{\boldsymbol{v}}}{c\|\boldsymbol{p}_0 - \boldsymbol{p}_{\mathrm{b}}\|}, \quad (87)$$

$$\psi_{\mathrm{s}} = \frac{\|\boldsymbol{v}\|(\boldsymbol{p}_0 - \boldsymbol{p}_{\mathrm{s}})^{\mathsf{T}}\vec{\boldsymbol{v}}}{c\|\boldsymbol{p}_0 - \boldsymbol{p}_{\mathrm{s}}\|} - \frac{(\boldsymbol{p}_0 - \boldsymbol{p}_{\mathrm{s}})^{\mathsf{T}}(\boldsymbol{v}_{\mathrm{LEO}} - \boldsymbol{v}_{\mathrm{E}})}{c\|\boldsymbol{p}_0 - \boldsymbol{p}_{\mathrm{s}}\|}, \quad (88)$$

[8]A typical value for η is 1ppm, and in case of the UE moving with 80 kph and satellite elevation angle being $\pi/4$, $|\psi_{\mathrm{b}}|$ and $|\psi_{\mathrm{s}}|$ are in the order of 10^{-6} and 10^{-5} respectively.

according to (12) and (14a) where $\vec{\boldsymbol{v}} = \boldsymbol{v}/\|\boldsymbol{v}\|$. Then using estimated $\hat{\boldsymbol{p}}_0$, $\hat{\gamma}_{\mathrm{b}}$ and γ_{s}, we can find $\|\hat{\boldsymbol{v}}\|$ and $\hat{\eta}$ as

$$\hat{\eta} = \frac{\hat{\gamma}_s - ((\hat{\psi}_{N,\mathrm{s}}/\hat{\psi}_{N,\mathrm{b}})\hat{\gamma}_b - \tilde{\psi}_{\mathrm{s}})}{1 - ((\hat{\psi}_{N,\mathrm{s}}/\hat{\psi}_{N,\mathrm{b}}) - \tilde{\psi}_{\mathrm{s}})}, \quad (89)$$

$$\|\hat{\boldsymbol{v}}\| = \frac{\hat{\gamma}_b - \hat{\eta}}{(1-\hat{\eta})\hat{\psi}_{N,\mathrm{b}}}, \quad (90)$$

where

$$\tilde{\psi}_{\mathrm{s}} = \frac{(\hat{\boldsymbol{p}}_0 - \boldsymbol{p}_{\mathrm{s}})^{\mathsf{T}}(\boldsymbol{v}_{\mathrm{LEO}} - \boldsymbol{v}_{\mathrm{E}})}{c\|\hat{\boldsymbol{p}}_0 - \boldsymbol{p}_{\mathrm{s}}\|}, \quad (91)$$

$$\hat{\psi}_{N,\mathrm{s}} = \frac{(\hat{\boldsymbol{p}}_0 - \boldsymbol{p}_{\mathrm{s}})^{\mathsf{T}}\vec{\boldsymbol{v}}}{c\|\hat{\boldsymbol{p}}_0 - \boldsymbol{p}_{\mathrm{s}}\|}, \quad (92)$$

$$\hat{\psi}_{N,\mathrm{b}} = \frac{(\hat{\boldsymbol{p}}_0 - \boldsymbol{p}_{\mathrm{b}})^{\mathsf{T}}\vec{\boldsymbol{v}}}{c\|\hat{\boldsymbol{p}}_0 - \boldsymbol{p}_{\mathrm{b}}\|}. \quad (93)$$

Here, the vector $\vec{\boldsymbol{v}}$ denotes the known UE's heading and the subscript N in (92) and (93) stands for normalized, with respect to the UE's speed. These estimates can be further improved using gradient descent applied to the relevant cost functions.

C. Complexity Analysis

In this subsection, the proposed simplified estimators are compared in terms of computational complexity, summarized in Table IV. Assuming a fixed number of grids G in each dimension, and I iterations for the quasi-Newton algorithm, the channel parameter estimation for the model Comm has the lowest complexity at $\mathcal{O}(GNM+G^2M+I(N+M))$. Here, the first term corresponds to the complexity of estimating the BS and satellite delays; the second term represents the complexity of 2D AoD estimation and the final term accounts for the refinement cost. The estimator for the model SlowD has a complexity of $\mathcal{O}(GM+GP+GNM+G^2M+I(N+M))$ where the terms respectively represent the complexity of satellite Doppler estimation, BS Doppler estimation, BS and satellite delay estimation, AoD estimation, and refinement. For the model CCFODnoICI, the complexity is given as $\mathcal{O}(N^2+GM+GP+GNM+G^2M+I(N+M))$. The first term reflects the additional cost of considering intersubcarrier Doppler effect term in satellite Doppler estimation, while the remaining terms are analogous to those in the model SlowD. Finally, model CCFOD has the highest complexity at $\mathcal{O}(N^2+GM+NM+GP+GNM+G^2M+IN^2M)$ Here, the third term represents the complexity of reconstructing the BS path, while the other terms are similar to the model CCFODnoICI, with the refinement step contributing $\mathcal{O}(IN^2M)$, due to the inclusion of ICI in this model. We note that algorithmic optimization and parallelization can affect the complexity, but will not significantly impact the complexity order.

V. Simulation Results

In this section, we illustrate the performance of our estimators based on different models considering the data generated from the generative model in (23). The objective of the simulations is not to reveal unexpected behaviors, but to determine *when each simplified model achieves performance comparable to the full model*. This provides quantitative guidance on selecting the least complex estimator that satisfies accuracy requirements in TN-NTN deployments.

TABLE IV
ASYMPTOTIC COMPUTATIONAL COMPLEXITY OF THE PROPOSED CHANNEL-PARAMETER ESTIMATORS. HERE, G DENOTES THE NUMBER OF GRID POINTS PER DIMENSION, N THE NUMBER OF SUBCARRIERS, M THE NUMBER OF OFDM SYMBOLS, P THE NUMBER OF BEAMFORMER PHASE REPETITIONS, AND I THE NUMBER OF QUASI-NEWTON ITERATIONS.

Model	**Complexity order**	**Elapsed time in seconds**
Comm	$\mathcal{O}\big(GNM + G^2M + I(N+M)\big)$	1.1
SlowD	$\mathcal{O}\big(GP + GNM + G^2M + I(N+M)\big)$	1.7
CCFODnoICI	$\mathcal{O}\big(N^2 + GP + GNM + G^2M + I(N+M)\big)$	2.9
CCFOD	$\mathcal{O}\big(N^2 + GP + GNM + G^2M + IN^2M\big)$	64.5

TABLE V
SIMULATIONS PARAMETERS

Parameter	**Symbol**	**Value**
Carrier frequency	f_c	2 GHz
Speed of light	c	3×10^8 m/s
Number of subcarriers	N	3300
Subcarrier spacing	Δ_f	30 kHz
Total symbol duration	T_s	35.7 μs
Symbol duration	T_0	33.3 μs
Cyclic prefix duration	T_{cp}	2.3 μs
Number of symbols	M	64
Number of antennas	L	64
LEO satellite velocity	$\|\boldsymbol{v}_{\text{s}}\|$	7800 m/s
Number of beamformer phase repetition	P	4
LEO satellite altitude	h	600 km
Earth rotation velocity	$\|\boldsymbol{v}_{\text{E}}\|$	465 m/s
Earth radius	R	6371 km
BS position	$\boldsymbol{p}_{\text{b}}$	$[0, 0, 5]^{\mathsf{T}}$ m
UE initial position	$\boldsymbol{p}_0$	$[20, 50, 1.5]^{\mathsf{T}}$ m
UE heading	$\vec{\boldsymbol{v}}$	$[1, 0, 0]^{\mathsf{T}}$ m/s

A. Simulation Setup and Theoretical Bounds

The system parameters are given in Table V. The time-varying channel gains $\alpha_{\text{b}}(t)$ and $\alpha_{\text{s}}(t)$ are modeled based on free space path-loss (FSPL) and given by $\alpha_{\text{b}}(t) = \sqrt{\cos^q(\boldsymbol{\theta}_{\text{el}}(t))}\lambda/(4\pi\|\boldsymbol{p}(t) - \boldsymbol{p}_{\text{b}}\|)$, where $q = 0.57$ [37, Sec. 9.7.3] and $\alpha_{\text{s}}(t) = \lambda/(4\pi\|\boldsymbol{p}(t) - \boldsymbol{p}_{\text{s}}(t)\|)$.

We employ two theoretical bounds to evaluate estimation accuracy. The first is the CRB, which represents the minimum achievable variance of an unbiased estimator when the estimation model perfectly matches the true data generation model. However, since the estimators in our scenario are not designed based on the generative model, achieving the CRB is not guaranteed in the presence of significant model mismatch. To address this, we utilize the MCRB as an alternative theoretical bound [38], [39]. The MCRB provides a lower bound on the variance of estimators under model mismatch and incorporates the effect of estimator bias. The CRB provides a reasonable bound for our mismatched model in the low to medium SNR regime, where estimation errors are mostly due to noise rather than model mismatches. At high SNR, however, the MCRB becomes more relevant, as the bias term dominates the bound while the variance term approaches zero, making it the appropriate theoretical bound in this regime. Thus, the CRB characterizes the low to medium SNR regime where noise dominates, while the MCRB bias term reflects the high SNR behavior, and therefore the full MCRB does not need to be explicitly plotted. The adoption of these bounds in our problem is elaborated in Appendix C and can support model selection based on the desired performance-complexity trade-off.

B. Results and Discussion

1) Mismatched Estimation Performance: First, we analyze the root mean-squared error (RMSE), CRB and bias terms of estimated UE's position for all simplified models, considering data generated from the true model versus received signal-to-noise ratio (SNR). To better understand the effect of BS and satellite transmit power, two figures are presented to illustrate the trends: Fig. 2 shows the case where the satellite transmit power is fixed at $P_{\text{s}} = 65$ dBm, while Fig. 3 depicts the case where the BS transmit power is fixed at $P_{\text{b}} = 35$ dBm. [9] In Fig. 2 the BS transmit power changes from -40 dBm to 50 dBm, and in Fig. 3 the satellite transmit power changes from 10 dBm to 80 dBm. In both figures, the velocity magnitude is set to $\|\boldsymbol{v}\| = 15$ kph, the CFO is $\eta = 10^{-8}$ and the satellite is located at an elevation angle of $\boldsymbol{\theta}^{\text{s}}_{\text{el}} = 88°$. It is observed that the CRB for all four models coincides exactly in both figures. The reason is that the combined Doppler and CFO (γ_b and γ_s) contains marginal position information compared to the other channel-domain parameters τ_s, τ_b and $\boldsymbol{\theta}$. The performance of the Comm and SlowD models is very similar, indicating that while accounting for slow-time Doppler is expected to improve AoD estimation and consequently positioning, its impact is overshadowed by the absence of inter-subcarrier Doppler compensation in this scenario. This observation is further reinforced by the performance improvement seen in the CCFODnoICI model compared to Comm and SlowD. The performance of models CCFODnoICI and CCFOD approaches the CRB at high SNR, showing importance of compensating for inter-subcarrier Doppler effect. In contrast, a significant gap is observed between the bias of models Comm and SlowD and the CRB at high SNR, highlighting that the performance of these two models is limited by model mismatch. Notably, except for high SNR, the performance of the CCFODnoICI and CCFOD models is similar, indicating that accounting for ICI has a negligible impact in this scenario at lower SNRs. However, the difference becomes more noticeable at high SNR.

The analyses presented above apply to the specific scenario described. In the following subsections, different scenarios are explored to provide a deeper understanding of the behavior of our algorithm.

2) Impact of CFO: In Fig. 4, the positioning performance of the four models is analyzed as a function of the CFO. For

[9]Here, P_{s} and P_{b} denote the effective isotropic radiated power (EIRP) of the satellite and BS, respectively. This is because the channel gains $\alpha_b(t)$ and $\alpha_s(t)$ do not include the antenna gains. According to [40], the S-band, 600 km altitude Set-2 configuration, the satellite EIRP density is approximately 28 dBW/MHz. Considering our bandwidth of approximately 100 MHz, this corresponds to ≈ 78 dBm total EIRP, therefore the choice $P_{\text{s}} = 65$ dBm is practical.

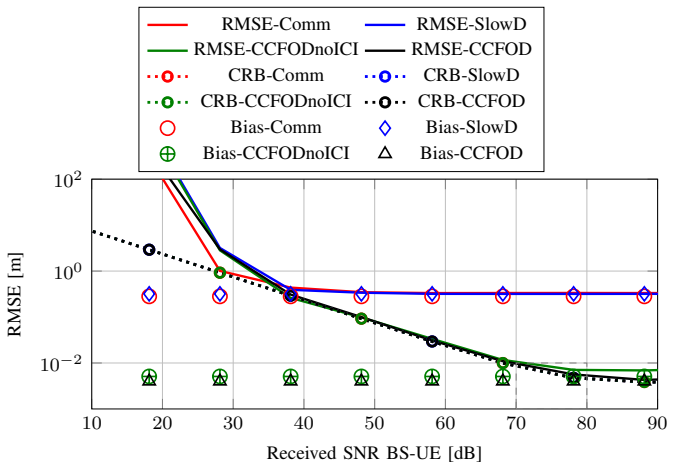


Fig. 2. RMSE and CRB of estimated position vs. received SNR in BS-UE path. All four CRB curves overlap in this figure (as in all subsequent figures), which is why they appear as a single curve. Comm and SlowD RMSE curves, as well as CCFODnoICI and CCFOD RMSE curves, overlap for medium–high received SNR. Since the legends in all figures are similar to that of Fig. 2, they are omitted in the subsequent figures for clarity. Bias values are included where relevant and omitted otherwise.

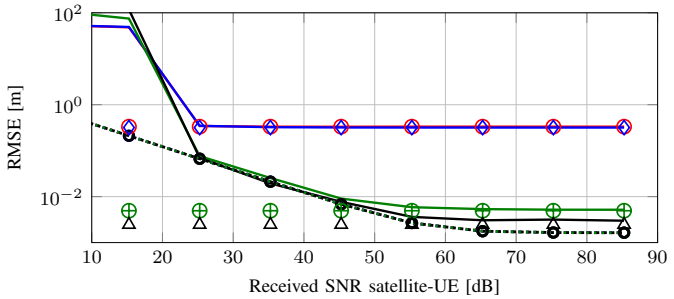


Fig. 3. RMSE and CRB of estimated position vs. received SNR in the satellite-UE path.Comm and SlowD RMSE curves overlap for medium–high received SNR.

this evaluation, the satellite is positioned at the zenith, and the user is assumed to be stationary. The transmit powers of the BS and satellite are set to $P_{\mathrm{b}} = 35$ dBm and $P_{\mathrm{s}} = 65$ dBm, respectively. The positioning CRB for all four models coincides, as expected, and all models achieve the CRB at low values of η. Therefore, the bias term is only presented for cases where the RMSE deviates from the CRB. By increasing η, model Comm, then model SlowD and model CCFODnoICI would introduce large estimation errors, but it is model CCFOD that takes the CFO into account in the ICI term as well as in modified Fourier matrix $\mathbf{F}_{\mathrm{s}}(\gamma_{\mathrm{s}})$, therefore, it is more robust towards CFO variations compared to the other models. The reason is that model Comm entirely ignores the presence of CFO, making it the most susceptible to CFO variations among all models. In contrast, the other models account for CFO to some extent, enabling them to tolerate higher CFO values. Among these, model CCFOD demonstrates the highest robustness. An important observation is that for higher values of CFO, the CCFOD model still achieves performance close to the CRB, resulting in centimeter-level positioning accuracy. This indicates that even for large CFO values, a complex estimation algorithm incorporating time-varying AoDs and second-order terms is not necessary. Instead, our most advanced estimation algorithm is sufficient to achieve centimeter-level positioning accuracy. In case more relaxed requirements on positioning

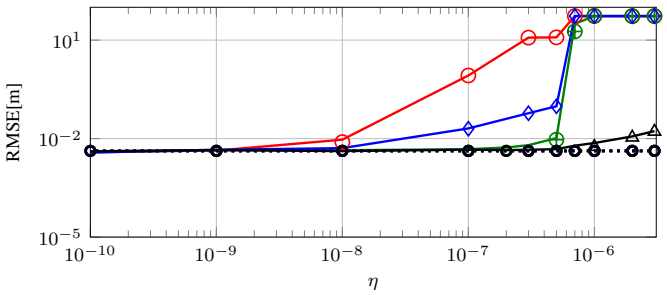


Fig. 4. RMSE and CRB of estimated position vs. CFO.

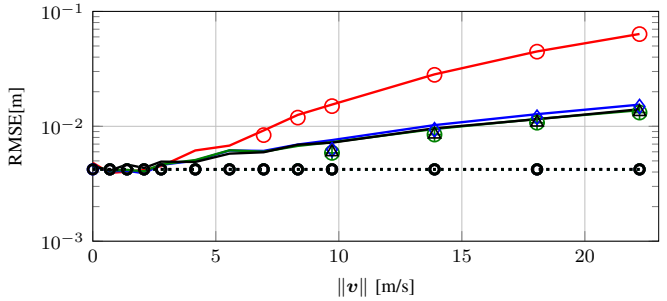


Fig. 5. RMSE and CRB of estimated position vs. UE's speed $\|\boldsymbol{v}\|$. The RMSE curves of SlowD, CCFODnoICI, and CCFOD lie almost on top of each other, with SlowD slightly higher than CCFODnoICI, and CCFOD slightly lower, as expected.

accuracy, other simplified models could be used.

3) Impact of UE Speed: In Fig. 5, the behavior of our four models is analyzed with varying speeds. We consider $\eta = 0$ in this scenario and the satellite is located at the zenith with the transmit powers of the BS and satellite set to $P_{\mathrm{b}} = 35$ dBm and $P_{\mathrm{s}} = 65$ dBm, respectively. Model Comm performs poorly when the velocity is as low as 3 m/s, as expected. In contrast, the other three models demonstrate strong robustness to variations in velocity due to the inclusion of γ_b and γ_s in their models. It is important to note that the impact of CFO and radial velocity is conveyed through Doppler shifts, making their effects similar when the satellite is located at the zenith and we investigate the effect of either CFO or radial velocity individually. Specifically in such case, the positioning accuracy when the UE's speed is 15 m/s is comparable to that when $\eta = 15/(3\times10^8) \approx 0.5\times10^{-7}$. Therefore, for practical values of the UE's speed, since the difference between models SlowD, CCFODnoICI and CCFOD is marginal, and model SlowD is sufficient.

4) Impact of Satellite Elevation: Fig. 6 demonstrates the behavior of our models versus satellite elevation angles. The UE is assumed to be stationary, with $\eta = 0$ and the transmit powers of the BS and satellite are fixed at $P_{\mathrm{b}} = 35$ dBm and $P_{\mathrm{s}} = 65$ dBm, respectively. It turns out that when the satellite is directly overhead, i.e. at $\boldsymbol{\theta}^{\mathrm{s}}_{\mathrm{el}} = \pi/2$, all four models perform very close to the CRB. The reason is that at $\boldsymbol{\theta}^{\mathrm{s}}_{\mathrm{el}} = \pi/2$, the satellite-UE relative motion is almost entirely orthogonal to the LoS direction. This makes the radial velocity nearly zero, and therefore the first-order Doppler term γ_{s} becomes negligible. Although the Doppler rate μ_{s} can be non-zero and may even reach its maximum near zenith (Appendix B), its effect over one OFDM block is much smaller than that of γ_{s}. Moreover, $\gamma_{\mathrm{b}} = 0$ and $\epsilon_{\mathrm{b}} = 0$ as the UE is stationary. Therefore, since the dominant source of model mismatch is the first-order

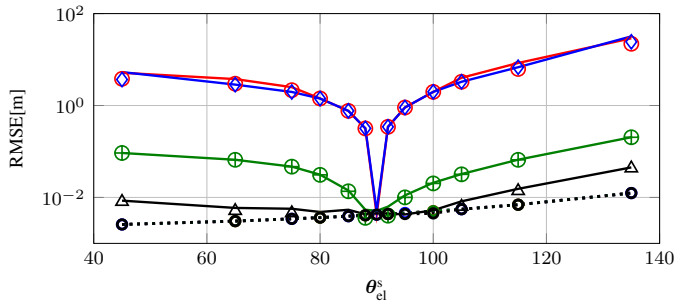


Fig. 6. RMSE and CRB of estimated position vs. satellite elevation angle.

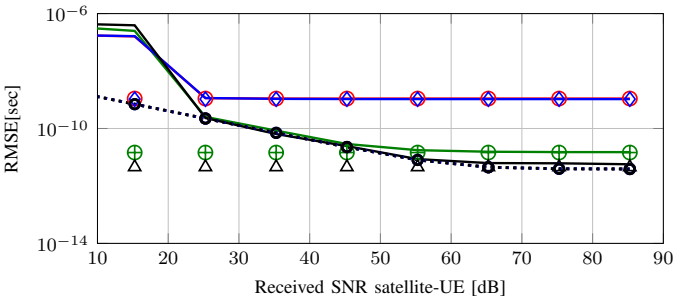


Fig. 7. RMSE and CRB of estimated $\Delta_{t,0}$ vs. received SNR. Comm and SlowD RMSE curves overlap for medium–high received SNR.

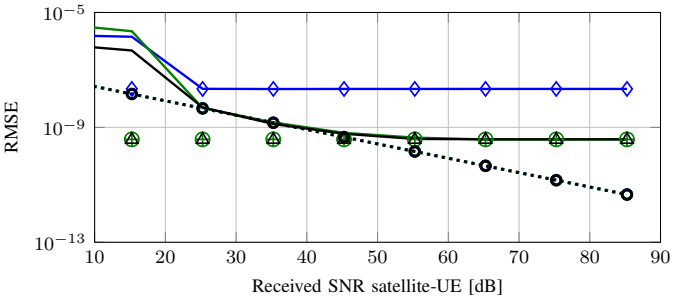


Fig. 8. RMSE and CRB of estimated η vs. received SNR. CCFODnoICI and CCFOD RMSE curves overlap for medium–high received SNR.

Doppler distortion rather than the second-order Doppler rate, all simplified models align closely with the generative model at $\boldsymbol{\theta}^{\mathrm{s}}_{\mathrm{el}} = \pi/2$, resulting in the lowest estimation error and all four models perform well when $\boldsymbol{\theta}^{\mathrm{s}}_{\mathrm{el}} = \pi/2$. However, as the satellite elevation angle deviates from $\pi/2$, the performance of models Comm and SlowD deteriorates. Model Comm performs poorly because it entirely neglects γ_s, which increases rapidly as the satellite moves away from the zenith. While model SlowD accounts for γ_s, it only considers it in the slow-time domain, leaving delay estimation across subcarriers susceptible to errors. In contrast, models CCFODnoICI and CCFOD consider inter-subcarrier Doppler effects, which spans over the slow time as well as the subcarrier domains. By estimating γ_s and compensating for these terms, models CCFODnoICI and CCFOD significantly outperform models Comm and SlowD.

It is worth noting that γ_s increases as the satellite elevation angle diverges further from the zenith. According to (33), a larger γ_s causes the first term in $\mathbf{F}^q_{\mathrm{s}}(\gamma_{\mathrm{s}}, \epsilon_{\mathrm{s}})$ to diverge more substantially from the IDFT matrix, due to the fast-time Doppler effect. In models Comm, SlowD and CCFODnoICI, the IDFT matrix is used to separate BS-UE and satellite-UE contributions based on (50), (51), and (52). This divergence makes it increasingly challenging for the estimators to separate the BS-UE path from the satellite-UE path, ultimately degrading localization performance, whereas model CCFOD (41) considers the first term in $\mathbf{F}_{\mathrm{s}}(\gamma_{\mathrm{s}})$ which is the dominant term in $\mathbf{F}^q_{\mathrm{s}}(\gamma_{\mathrm{s}}, \epsilon_{\mathrm{s}})$ for satellite elevation angle away from zenith.

Remark 3. *In general, the choice of the appropriate estimation algorithm depends on factors such as the required positioning accuracy, the expected scenario, and the complexity preferences. Sec. V-B2 to V-B4 provide a general overview of how different models perform in various scenarios, and the results can serve as a guideline for model selection.*

5) Estimation Performance of Other Parameters: Finally, the estimation performance of $\Delta_{t,0}$, η and $\|\boldsymbol{v}\|$ are illustrated in Figs. 7, 8, and 9, respectively. The UE velocity is set to 15 kph, the BS transmit power is set to $P_{\mathrm{b}} = 35$ dBm, with $\Delta_{t,0} = 1$ ns, $\eta = 10^{-8}$ and the satellite positioned at an elevation angle of $\boldsymbol{\theta}^{\mathrm{s}}_{\mathrm{el}} = 88°$, which is the simulation scenario as the one used in Fig. 3. In Fig. 7, models Comm and SlowD exhibit similar behavior, while model CCFODnoICI outperforms them, with model CCFOD almost achieving the CRB. As for estimation performance of η and $\|\boldsymbol{v}\|$ in Figs. 8–9, models CCFODnoICI and CCFOD perform similarly and outperform model SlowD as expected and model Comm is not included since it is not capable of estimating η and $\|\boldsymbol{v}\|$.

By comparing Figs. 8–9 with Fig. 3, it can be observed that the second-order terms become significant at high SNR, but and only in the estimation of η and $\|\boldsymbol{v}\|$. This is due to the fact that while Doppler conveys negligible positioning information, it conveys significant information for estimating η and $\|\boldsymbol{v}\|$ and specifically the second-order terms (derived based on time-varying Doppler) will be crucial only when we operate at high SNR and we aim at estimating η and $\|\boldsymbol{v}\|$ with very high accuracy. Based on Figs. 8–9, our CCFODnoICI and CCFOD models would achieve speed and CFO estimation accuracies of sub-1 m/s and sub-0.1 ppm respectively, therefore as long as these values meet the requirements of our application, there is no need to incorporate second-order terms.

VI. Concluding Remarks

This paper presented a comprehensive study on localization, velocity magnitude estimation, and synchronization for a mobile UE in integrated cellular and non-terrestrial networks. We derived a generative model that accounts for the time-varying Doppler and path gains effect, forming the foundation for understanding the positioning system's behavior. Building upon

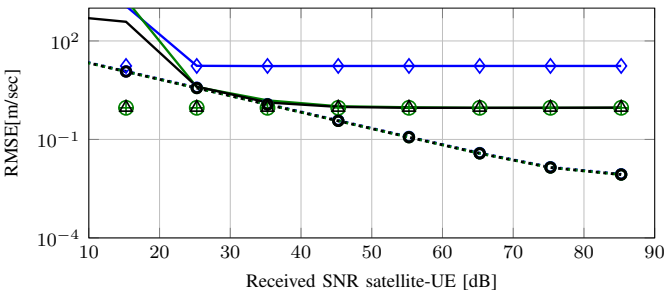


Fig. 9. RMSE and CRB of estimated $\|\boldsymbol{v}\|$ vs. received SNR. CCFODnoICI and CCFOD RMSE curves overlap for medium–high SNR.

this, we proposed a hierarchy of four simplified models, each offering a distinct trade-off between computational complexity and performance. Estimation algorithms were developed for all the models, enabling accurate estimation of position, velocity magnitude, initial clock bias, and carrier frequency offset. Through rigorous simulations, we demonstrated the effectiveness of the proposed models across diverse scenarios. By analyzing both the performance and complexity of each model, we can strategically select the most suitable one for different deployment conditions, optimizing processing power while maintaining high accuracy. These insights offer practical guidance for improving 6G positioning and synchronization in mobile scenarios, facilitating the seamless integration of NTNs into future wireless networks.

Extensions of this work could focus on the comparative quantitative evaluation of integrated terrestrial and NTN positioning to pure terrestrial or pure NTN solutions, to better understand trade-off in terms of metrics such as complexity, performance, coverage, latency.

ACKNOWLEDGMENT

The authors gratefully acknowledge the support of Volvo AB.

APPENDIX A
DERIVATION OF CONTINUOUS-TIME GENERATIVE MODEL

Following (3), (2) and (1), $\tilde{y}_{\mathrm{b}}(t)$ can be written as

$$\tilde{y}_{\mathrm{b}}(t) = \alpha_{\mathrm{b}}(t)\Re\Big\{\sum_{l=1}^{L}\tilde{z}_{\mathrm{b},l}(t-\tau^p_{\mathrm{b},l}(t))\Big\} \tag{94}$$

$$= \alpha_{\mathrm{b}}(t)\Re\Big\{\sum_{l=1}^{L} w_l(t-\tau^p_{\mathrm{b},l}(t))x_{\mathrm{b}}(t-\tau^p_{\mathrm{b},l}(t))e^{j2\pi f_c(t-\tau^p_{\mathrm{b},l}(t))}\Big\}.$$

where $w_l(t) = [\boldsymbol{w}(t)]_l$ and $\tilde{z}_{\mathrm{b},l}(t) = [\tilde{\boldsymbol{z}}_{\mathrm{b}}(t)]_l$. Then,

$$\tilde{y}_{\mathrm{b}}(t) \tag{95}$$

$$= \Re\{\alpha_{\mathrm{b}}(t)\boldsymbol{a}^{\mathsf{T}}(\boldsymbol{\theta}(t))\boldsymbol{w}(t-\tau^p_{\mathrm{b}}(t))x_{\mathrm{b}}\left(t-\tau^p_{\mathrm{b}}(t)\right)e^{j2\pi f_c\left(t-\tau^p_{\mathrm{b}}(t)\right)}\}.$$

APPENDIX B
LINEARIZING THE DELAY PROPAGATION

We express the propagation delay as

$$\tau(t) = \frac{r(t)}{c} = \frac{\|\boldsymbol{p}(t)-\boldsymbol{p}_i(t)\|}{c}, \tag{96}$$

where $i \in \mathrm{b},\mathrm{s}$ denotes the transmitter (either the BS or the satellite). The transmitter trajectory is modeled as $\boldsymbol{p}_i(t) = \boldsymbol{p}_i + \boldsymbol{v}_i t$, with $\boldsymbol{p}_i$ and $\boldsymbol{v}_i$ representing its initial 3D position and velocity, respectively. Similarly, the receiver trajectory is given by $\boldsymbol{p}(t) = \boldsymbol{p}_0 + \boldsymbol{v}t$, where $\boldsymbol{p}_0$ and $\boldsymbol{v}$ denote the initial 3D position and velocity of the receiver. Substituting the trajectories into (96), the propagation delay can be equivalently rewritten as

$$\tau(t) = \frac{\|\boldsymbol{p}_0 + \boldsymbol{v}_{i,\mathrm{u}}t - \boldsymbol{p}_i\|}{c}, \tag{97}$$

where $\boldsymbol{v}_{i,\mathrm{u}}$ denotes the relative velocity between the transmitter and the receiver. Let's expand the nominator of (96)

$$\|\boldsymbol{p}_0 + \boldsymbol{v}_{i,\mathrm{u}}t - \boldsymbol{p}_i\| = \|\boldsymbol{p}_0 - \boldsymbol{p}_i\|\frac{\|\boldsymbol{p}_0 + \boldsymbol{v}_{i,\mathrm{u}}t - \boldsymbol{p}_i\|}{\|\boldsymbol{p}_0 - \boldsymbol{p}_i\|} \tag{98}$$

$$= \|\boldsymbol{p}_0 - \boldsymbol{p}_i\|\sqrt{\frac{(\boldsymbol{p}_0 + \boldsymbol{v}_{i,\mathrm{u}}t - \boldsymbol{p}_i)^{\mathsf{T}}(\boldsymbol{p}_0 + \boldsymbol{v}_{i,\mathrm{u}}t - \boldsymbol{p}_i)}{\|\boldsymbol{p}_0 - \boldsymbol{p}_i\|^2}}$$

$$= \|\boldsymbol{p}_0 - \boldsymbol{p}_i\|\sqrt{1 + \frac{2(\boldsymbol{p}_0 - \boldsymbol{p}_i)^{\mathsf{T}}\boldsymbol{v}_{i,\mathrm{u}}t + \|\boldsymbol{v}_{i,\mathrm{u}}t\|^2}{\|\boldsymbol{p}_0 - \boldsymbol{p}_i\|^2}}. \tag{99}$$

Let's assume that the UE and transmitter displacement during the entire transmission block is much smaller than their initial distance, which is equivalent to the stop-and-hop assumption [41, Ch. 2.7.2]. Then, we can conclude that [10]

$$2(\boldsymbol{p}_0 - \boldsymbol{p}_i)^{\mathsf{T}}\boldsymbol{v}_{i,\mathrm{u}}MT_s + \|\boldsymbol{v}_{i,\mathrm{u}}MT_s\|^2 \ll \|\boldsymbol{p}_0 - \boldsymbol{p}_i\|^2. \tag{100}$$

We can then expand (99) using the Taylor approximation $\sqrt{1+x} \approx 1 + \frac{x}{2} - \frac{x^2}{8}$ for small x, keeping all constant, linear-in-t, and quadratic-in-t terms:

$$\begin{aligned}
&\|\boldsymbol{p}_0 + \boldsymbol{v}_{i,\mathrm{u}}t - \boldsymbol{p}_i\| \approx \|\boldsymbol{p}_0 - \boldsymbol{p}_i\|\times \\
&\left(1 + \frac{t(\boldsymbol{p}_0 - \boldsymbol{p}_i)^{\mathsf{T}}\boldsymbol{v}_{i,\mathrm{u}} + 1/2(\|\boldsymbol{v}_{i,\mathrm{u}}t\|^2 - v_{i,\mathrm{u}}^2t^2)}{\|\boldsymbol{p}_0 - \boldsymbol{p}_i\|^2}\right) \\
&= \|\boldsymbol{p}_0 - \boldsymbol{p}_i\| + \frac{t(\boldsymbol{p}_0 - \boldsymbol{p}_i)^{\mathsf{T}}\boldsymbol{v}_{i,\mathrm{u}} + 1/2(\|\boldsymbol{v}_{i,\mathrm{u}}t\|^2 - v_{i,\mathrm{u}}^2t^2)}{\|\boldsymbol{p}_0 - \boldsymbol{p}_i\|} \\
&= \|\boldsymbol{p}_0 - \boldsymbol{p}_i\| + v_{i,\mathrm{u}}t + 1/2a_{i,\mathrm{u}}t^2.
\end{aligned} \tag{101}$$

where $v_{i,\mathrm{u}} = (\boldsymbol{p}_0 - \boldsymbol{p}_i)^{\mathsf{T}}\boldsymbol{v}_{i,\mathrm{u}}/\|\boldsymbol{p}_0 - \boldsymbol{p}_i\|$ is the initial radial velocity, and the second-order term denotes the quadratic changes in the radial distance which can be interpreted as the radial pseudo-acceleration $a_{i,\mathrm{u}} = (\|\boldsymbol{v}_{i,\mathrm{u}}\|^2 - v_{i,\mathrm{u}}^2)/\|\boldsymbol{p}_0 - \boldsymbol{p}_i\|$. Therefore, with the above approximation, the radial distance can be written as a constant acceleration kinematic equation, and the radial velocity and the delay will be approximated as

$$\begin{aligned}
v_{i,\mathrm{u}}(t) &= v_{i,\mathrm{u}} + a_{i,\mathrm{u}}t, \\
\tau(t) &= r(t)/c = \tau_0 + \psi_0 t + 1/2\mu t^2,
\end{aligned} \tag{102}$$

where $\tau_0 = \|\boldsymbol{p}_0 - \boldsymbol{p}_i\|/c$ is the initial delay, $\psi_0 = v_{i,\mathrm{u}}/c$ is the initial normalized Doppler shift and $\mu = a_{i,\mathrm{u}}/c$ is the normalized Doppler shift rate.

APPENDIX C
FIM AND BIAS TERM IN MRCB

The positional parameters are as follows for the model Comm

$$\boldsymbol{\chi}^a_{\mathrm{pos}} = [\alpha_{\mathrm{R,b}}, \alpha_{\mathrm{I,b}}, \alpha_{\mathrm{R,s}}, \alpha_{\mathrm{I,s}}, \boldsymbol{p}_0^{\mathsf{T}}, \Delta_{t,0}]^{\mathsf{T}} \in \mathbb{R}^8, \tag{103}$$

while for models k = SlowD, CCFODnoICI, and CCFOD, they are

$$\boldsymbol{\chi}^{\mathrm{Comm}}_{\mathrm{pos}} = [\boldsymbol{\chi}^{\mathrm{Comm}\,\mathsf{T}}_{\mathrm{pos}}, \|\boldsymbol{v}\|, \eta]^{\mathsf{T}} \in \mathbb{R}^{10} \tag{104}$$

The performance bounds Fisher information matrix (FIM) and bias in MCRB are detailed here. As a basic bound, we use FIM, which is given by [42]

$$\mathbf{F}_{\mathrm{ch}} = \frac{2}{\sigma^2}\sum_{m=0}^{M-1}\sum_{n=0}^{N-1}\Re\Big\{\frac{\partial[\boldsymbol{R}]_{n,m}}{\partial\boldsymbol{\chi}^k_{\mathrm{ch}}}\left(\frac{\partial[\boldsymbol{R}]_{n,m}}{\partial\boldsymbol{\chi}^k_{\mathrm{ch}}}\right)^{\mathsf{H}}\Big\}, \tag{105}$$

in which $\boldsymbol{R} \in \mathbb{C}^{N\times M}$ is the noise-free part of the received signal, $\boldsymbol{\chi}^k_{\mathrm{ch}} \in \mathbb{R}^8$ in case of evaluating model Comm (k = Comm) and $\boldsymbol{\chi}^k_{\mathrm{ch}} \in \mathbb{R}^{10}$ (53) in case of evaluating model SlowD, CCFODnoICI, and CCFOD (k = SlowD, CCFODnoICI, CCFOD) (65). We can convert $\mathbf{F}_{\mathrm{ch}}$ to the positional FIM, $\mathbf{F}_{\mathrm{pos}}$, corresponding to positional vector by using the Jacobian matrix $\mathbf{F}_{\mathrm{po}} = \boldsymbol{J}^{\mathrm{T}}\mathbf{F}_{\mathrm{ch}}\boldsymbol{J}$, where $\boldsymbol{J}$ is the Jacobian

[10] According to the parameter values in Table. V, for the BS-UE link with UE speed up to 80 km/h, the ratio between the left-hand side and right-hand side of (100) is approximately 1.9×10^{-3}, while for the satellite-UE link (worst case with satellite at initial elevation angle of $\boldsymbol{\theta}^{\mathrm{s}}_{\mathrm{el}} = \pi/4$) the ratio is approximately 1.9×10^{-6}.

matrix with elements $\boldsymbol{J}_{m,n} = \partial[\boldsymbol{\chi}_{\text{ch}}^k]_m / \partial[\boldsymbol{\chi}_{\text{ch}}^k]_n$. In case of $k = \text{Comm}$, $\boldsymbol{J} \in \mathbb{C}^{8\times 10}$ and in case of $k = \text{SlowD, CCFODnoICI, CCFOD}$, $\boldsymbol{J} \in \mathbb{C}^{10\times 10}$.

In case of mismatched estimation, we can find the positioning bias through MCRB for each model $k = \text{Comm, SlowD, CCFODnoICI, CCFOD}$ as

$$B_{\text{pos}}^k = \sqrt{\text{trace}((\hat{\boldsymbol{\chi}}_{\text{pos}[5:7]}^k)^{\mathsf{H}} \hat{\boldsymbol{\chi}}_{\text{pos}[5:7]}^k)}, \tag{106}$$

where

$$\hat{\boldsymbol{\chi}}_{\text{pos}}^k = \arg\min_{\boldsymbol{\chi}_{\text{pos}}^k} [\|\mathbf{Y}_{\text{NF}} - \mathbf{Y}_{\text{NF}}^k(\boldsymbol{\chi}_{\text{pos}}^k)\|^2]. \tag{107}$$

Here, $\mathbf{Y}_{\text{NF}}$ represents the noise-free received signal based on the generative model, $\mathbf{Y}_{\text{NF}}^k$ corresponds to the noise-free observations derived from the simplified models. The vector $\boldsymbol{\chi}_{\text{pos}}^k$ is given by (103) and (104). For models SlowD, CCFODnoICI, and CCFOD, the estimator bias for the magnitude of the initial clock bias, velocity, and CFO can be determined as $B_{\Delta_{t,0}} = |\hat{\boldsymbol{\chi}}_{\text{pos}[8]}^k|$, $B_{\|\boldsymbol{v}\|} = |(\hat{\boldsymbol{\chi}}_{\text{pos}[9]}^k|$, and $B_\eta = |\hat{\boldsymbol{\chi}}_{\text{pos}[10]}^k|$.

REFERENCES

[1] G. Araniti *et al.*, "Toward 6G non-terrestrial networks," *IEEE Netw.*, vol. 36, no. 1, pp. 113–120, Jan. 2022.

[2] W. Jiang *et al.*, "The road towards 6G: A comprehensive survey," *IEEE Open J. Commun. Soc.*, vol. 2, pp. 334–366, 2021.

[3] M. M. Azari *et al.*, "Evolution of non-terrestrial networks from 5G to 6G: A survey," *Commun. Surveys Tuts.*, vol. 24, no. 4, pp. 2633–2672, 2022.

[4] H. K. Dureppagari *et al.*, "NTN-based 6G localization: Vision, role of LEOs, and open problems," *Wireless Commun.*, vol. 30, no. 6, pp. 44–51, 2023.

[5] A. Guidotti *et al.*, "The path to 5G-advanced and 6G non-terrestrial network systems," in *Advanced Satellite Multimedia Systems Conference and Signal Processing for Space Communications Workshop (ASMS/SPSC)*. IEEE, 2022.

[6] Q. Wei *et al.*, "Energy-efficient caching and user selection for resource-limited sagins in emergency communications," *IEEE Trans. Commun.*, vol. 73, no. 6, pp. 4121–4136, 2025.

[7] Z. Jia *et al.*, "Service function chain dynamic scheduling in space-air-ground integrated networks," *IEEE Trans. Veh. Technol.*, vol. 74, no. 7, pp. 11 235–11 248, 2025.

[8] A. Behravan *et al.*, "Positioning and sensing in 6G: Gaps, challenges, and opportunities," *IEEE Veh. Tech. Mag.*, vol. 18, no. 1, pp. 40–48, Mar. 2022.

[9] S. Saleh *et al.*, "Integrated 6G TN and NTN localization: Challenges, opportunities, and advancements," *IEEE Comm. Stand. Mag.*, vol. 9, no. 2, pp. 63–71, 2025.

[10] R. Whiton, "Cellular localization for autonomous driving: A function pull approach to safety-critical wireless localization," *IEEE Veh. Tech. Mag.*, vol. 17, no. 4, pp. 28–37, Dec. 2022.

[11] J. A. del Peral-Rosado *et al.*, "Preliminary field results of a dedicated 5G positioning network for enhanced hybrid positioning," *Engineering Proceedings*, vol. 54, no. 1, p. 6, 2023.

[12] S. Dwivedi *et al.*, "Positioning in 5G networks," *IEEE Commun. Mag.*, vol. 59, no. 11, pp. 38–44, Nov. 2021.

[13] H. Li *et al.*, "Analysis of the synchronization requirements of 5G and corresponding solutions," *IEEE Comm. Stand. Mag.*, vol. 1, no. 1, pp. 52–58, Mar. 2017.

[14] J. A. del Peral-Rosado *et al.*, "Survey of cellular mobile radio localization methods: From 1G to 5G," *Commun. Surveys Tuts.*, vol. 20, no. 2, pp. 1124–1148, 2017.

[15] M. Neinavaie *et al.*, "Acquisition, Doppler tracking, and positioning with starlink LEO satellites: First results," *IEEE Trans. Aerosp. Electron. Syst.*, vol. 58, no. 3, pp. 2606–2610, 2021.

[16] I. Ali *et al.*, "Doppler characterization for LEO satellites," *IEEE Trans. Commun.*, vol. 46, no. 3, pp. 309–313, 1998.

[17] D.-R. Emenonye *et al.*, "Fundamentals of LEO-based localization," *IEEE Trans. Inf. Theory*, vol. 71, no. 7, pp. 5277–5311, 2025.

[18] M. Harounabadi *et al.*, "Toward integration of 6G-NTN to terrestrial mobile networks: Research and standardization aspects," *IEEE Wireless Commun.*, vol. 30, no. 6, pp. 20–26, Dec. 2023.

[19] G. Geraci *et al.*, "Integrating terrestrial and non-terrestrial networks: 3D opportunities and challenges," *IEEE Commun. Mag.*, vol. 61, no. 4, pp. 42–48, 2023.

[20] G. Charbit *et al.*, "Satellite and cellular networks integration-a system overview," in *Joint European Conference on Networks and Communications & 6G Summit (EuCNC/6G Summit)*, 2021, pp. 118–123.

[21] H. Sallouha *et al.*, "On the ground and in the sky: A tutorial on radio localization in ground-air-space networks," *IEEE Commun. Surv. Tuts.*, 2024.

[22] A. Gonzalez-Garrido *et al.*, "5G positioning reference signal configuration for integrated terrestrial/non-terrestrial network scenario," in *IEEE ION Position, Location and Navigation Symposium (PLANS)*, 2023, pp. 1136–1142.

[23] ——, "Interference analysis and modeling of positioning reference signals in 5G NTN," *IEEE Open J. Commun. Soc.*, vol. 5, pp. 7567–7581, Jan. 2024.

[24] T. Liang *et al.*, "Toward seamless localization and communication: A satellite-UAV NTN architecture," *IEEE Netw.*, vol. 38, no. 4, Jul. 2024.

[25] T. Jin *et al.*, "Fusion positioning of GNSS-cellular signals of opportunity under low observability," *IEEE Trans. Instrum. Meas.*, 2024.

[26] D.-R. Emenonye *et al.*, "Joint 9D receiver localization and ephemeris correction with LEO and 5G base stations," in *IEEE Military Communications Conference (MILCOM)*, 2024, pp. 330–335.

[27] F. Zhang *et al.*, "Joint range and velocity estimation with intrapulse and intersubcarrier Doppler effects for OFDM-based radcom systems," *IEEE Trans. Signal Process.*, vol. 68, pp. 662–675, 2020.

[28] R. Prasad, "OFDM for wireless communications systems," *Artech House Universal Personal Communications Library/Artech House*, 2004.

[29] W. J. Riley *et al.*, *Handbook of frequency stability analysis*. US Department of Commerce, National Institute of Standards and Technology, 2008.

[30] K. Keykhosravi *et al.*, "RIS-enabled SISO localization under user mobility and spatial-wideband effects," *IEEE J. Sel. Top. Signal Process.*, vol. 16, no. 5, pp. 1125–1140, 2022.

[31] T. ETSI, "138 211-v16. 2.0, 5G NR," *Physical channels and modulation (3GPP TS 38.211 version 16.2. 0 Release 16), ETSI*, 2020.

[32] V. Koivunen *et al.*, "Multicarrier ISAC: Advances in waveform design, signal processing, and learning under nonidealities," *IEEE Signal Process. Mag.*, vol. 41, no. 5, pp. 17–30, Sep. 2024.

[33] A. Alkhateeb *et al.*, "Frequency selective hybrid precoding for limited feedback millimeter wave systems," *IEEE Trans. Commun.*, vol. 64, no. 5, pp. 1801–1818, 2016.

[34] H. Wymeersch *et al.*, "Radio localization and sensing—part I: Fundamentals," *IEEE Commun. Lett.*, vol. 26, no. 12, pp. 2816–2820, 2022.

[35] M. K. Ercan *et al.*, "RIS-aided NLoS monostatic multi-target sensing under angle-Doppler coupling," *IEEE Trans. Veh. Technol.*, 2025.

[36] K. Keykhosravi *et al.*, "SISO RIS-enabled joint 3D downlink localization and synchronization," in *IEEE Int. Conf. Commun.*, 2021, pp. 1–6.

[37] W. L. Stutzman *et al.*, *Antenna theory and design*. John Wiley & Sons, 2012.

[38] S. Fortunati *et al.*, "Performance bounds for parameter estimation under misspecified models: Fundamental findings and applications," *IEEE Signal Process. Mag.*, vol. 34, no. 6, pp. 142–157, 2017.

[39] C. D. Richmond *et al.*, "Parameter bounds on estimation accuracy under model misspecification," *IEEE Trans. Signal Process.*, vol. 63, no. 9, pp. 2263–2278, 2015.

[40] "Solutions for NR to support non-terrestrial networks (NTN)," 3rd Generation Partnership Project (3GPP), Technical Report TR 38.821, Mar. 2023, available: https://www.3gpp.org/DynaReport/38821.htm.

[41] M. A. Richards *et al.*, *Fundamentals of radar signal processing*. Mcgraw-hill New York, 2022, vol. 1.

[42] S. M. Kay, *Fundamentals of statistical signal processing: estimation theory*. Prentice-Hall, Inc., 1993.



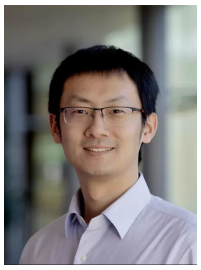
Yasaman Ettefagh received the Ph.D. degree in electrical engineering from Chalmers University of Technology, Gothenburg, Sweden. She is currently working as sensor fusion algorithm developer at Volve AB, Gothenburg, Sweden. She has worked as an RF optimization engineer at Ericsson from 2015 to 2017. Her research focuses on radio localization, wireless communication and signal processing.



Sharief Saleh (Member, IEEE) received the B.Sc. and M.Sc. degrees in electrical engineering from Qatar University, Doha, Qatar, in 2016 and 2018, respectively, and the Ph.D. degree in electrical and computer engineering at Queen's University, ON, Canada, in 2023. He is currently a Marie Skłodowska-Curie Actions (MSCA) Postdoctoral Fellow in the Department of Electrical Engineering at Chalmers University of Technology, Gothenburg, Sweden. His current research interests include 5G/6G positioning in terrestrial and non-terrestrial networks, channel modeling and estimation, and sensor fusion.



Musa Furkan Keskin (Member, IEEE) received the Ph.D. degree in Electrical and Electronics Engineering from Bilkent University, Ankara, Turkey, in 2018. He is currently a Researcher in the Department of Electrical Engineering at Chalmers University of Technology in Gothenburg, Sweden, where he is leading and contributing to various interdisciplinary and industry-focused research projects at both Swedish and European levels, with a specialization in integrated localization, communication and sensing in 6G systems. His awards include the 2019 IEEE Turkey Best Ph.D. Thesis Award for his work on visible light positioning systems, the EU MSCA Postdoctoral Fellowship for his project "OTFS-RADCOM: A New Waveform for Joint Radar and Communications Beyond 5G.", and, the Swedish Research Council (VR) Starting Grant for his project on "Localization and Sensing for Perceptive Cell-Free Networks Towards 6G". Dr. Keskin serves as an Associate Editor for the IEEE Transactions on Communications and IEEE Transactions on Mobile Computing.



Hui Chen (Member, IEEE) received the Ph.D. degree in electrical and computer engineering from King Abdullah University of Science and Technology, Saudi Arabia, in 2021. He is currently a Research Specialist with Chalmers University of Technology, Sweden. He is actively contributing to several EU projects (e.g., 6G-DISAC and HEXA-X), Swedish Vinnova, and VR projects in the field of localization and sensing. He is the recipient of the European Union Marie Skłodowska-Curie Postdoctoral Fellowship, the Swedish Vinnova International Mobility Grant, Chalmers Area-of-Advance Transport/ICT Seed Fundings, and the Ericsson Research Grant. His research focuses on 5G/6G localization and sensing, distributed ISAC, and machine learning.



Gonzalo Seco-Granados (Fellow, IEEE) received the Ph.D. degree in Telecommunications Eng. from the Univ. Politecnica de Catalunya in 2000, and the MBA degree from IESE Business School in 2002. From 2002 to 2005, he was with the European Space Agency. He is currently a Professor in the Dept. of Telecommunications at the Univ. Autonoma de Barcelona, and Director of the Center for Space Studies and Research. He is affiliated with the Institute of Space Studies of Catalonia and is an ICREA Academia Fellow. In 2015, 2019, and 2022, he was a Fulbright Visiting Scholar at the Univ. of California, Irvine, USA. His research interests encompass signal processing for GNSS, LEO-PNT, and 5G/6G integrated communications, localization, and sensing. He is a member of the EURASIP Signal Processing for Multisensor Systems TCsince 2022. He served as President of the Spanish Chapter of the IEEE AES Society (2018–2025). He received the 2021 IEEE SP Society's Best Paper Award.



Henk Wymeersch (Fellow, IEEE) obtained the Ph.D. degree in Electrical Engineering/Applied Sciences in 2005 from Ghent University, Belgium. He is currently a Professor of Communication Systems with the Department of Electrical Engineering at Chalmers University of Technology, Sweden and a Distinguished Visiting Professor at Tsinghua University. Prior to joining Chalmers, he was a postdoctoral researcher from 2005 until 2009 with the Laboratory for Information and Decision Systems at the Massachusetts Institute of Technology. Prof. Wymeersch served as Associate Editor for IEEE Communication Letters, IEEE Transactions on Wireless Communications, and IEEE Transactions on Communications and is currently Senior Member of the IEEE Signal Processing Magazine Editorial Board. During 2019-2021, he was an IEEE Distinguished Lecturer with the Vehicular Technology Society. His current research interests include the convergence of communication and sensing, in a 5G and Beyond 5G context.